Supplementary information to:

Secondary organic aerosol formation from sequential oxidation of toluene and cresols

Aliisa Ojala[1], Aurelien Le-Bayon[3], Avinash Kumar[1], Netta Vinkvist[2], Anni Savolainen[1], Anna Kervinen[1], Karine Sartelet[3], Matti Rissanen[1,2], Siddharth Iyer[1]

[1]Aerosol Physics Laboratory, Tampere University, FI-33101 Tampere, Finland

[2]Department of Chemistry, University of Helsinki, FI-00014 Helsinki, Finland

[3]CEREA, ENPC, Institut Polytechnique de Paris, EDF R\&D, IPSL, Marne la Vall'ee, France

Table of Contents

Computational

S1: OH-addition/H-abstraction

Autoxidation of cresols can be initiated by reactions with the OH radical [1]. Site-specific OH-addition and H-abstraction yields are studied using computational methods and presented below. Notation used is presented in Fig. S1.

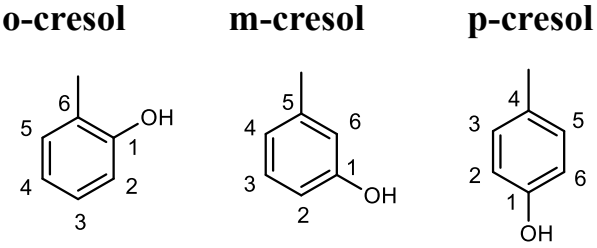

Fig. S1: Cresol isomers and OH interaction sites.

Bimolecular rate coefficients ($cm^3\ molecule^{-1}\ s^{-1}$) for OH-addition to cresols at ROHF-CCSD(T)-F12a/VDZ-F12/ωB97X-D/aug-cc-pVTZ level of theory (henceforth denoted as F12-level) are calculated using equation

$$k_{bimolec} = \frac{k_B T}{hc^{\circ}} \exp\left(\frac{G_{TS} - G_R}{k_B T}\right), \quad (1)$$

where k_B and h are Boltzmann's and Planck's constant respectively c° is the total concentration of molecules in the atmosphere in standard conditions, the temperature T is set to 298 K and G_{TS} and G_R are the Gibbs free energies of the transition state and reactant, respectively. The lowest energy conformers are used. For the H-abstraction from the OH group, a wavefunction stability check [7] was conducted by performing a rotation of the active space. This ensured that the lowest energy RHF input was found for the F12-level calculation. The results are presented in Table S1

Table S1: Bimolecular rate coefficients for OH-addition and H-abstraction ($cm^3\ molecule^{-1}\ s^{-1}$) at T=298.15 K

cresol	1	2	3	4	5	6	CH_3 abs	OH-abs*	total
ortho	$9.69{\cdot}10^{-14}$	$1.09{\cdot}10^{-12}$	$6.37{\cdot}10^{-15}$	$2.37{\cdot}10^{-14}$	$1.24{\cdot}10^{-14}$	$3.32{\cdot}10^{-13}$	$7.65{\cdot}10^{-14}$	**	$1.63{\cdot}10^{-12}$
meta	$1.52{\cdot}10^{-14}$	$9.26{\cdot}10^{-12}$	$1.93{\cdot}10^{-14}$	$6.13{\cdot}10^{-13}$	$7.53{\cdot}10^{-15}$	$2.26{\cdot}10^{-11}$	$1.14{\cdot}10^{-13}$	$1.22{\cdot}10^{-16}$	$3.26{\cdot}10^{-11}$
para	$1.08{\cdot}10^{-14}$	$8.98{\cdot}10^{-13}$	$1.52{\cdot}10^{-14}$	$1.99{\cdot}10^{-14}$	-	-	$2.38{\cdot}10^{-14}$	$7.56{\cdot}10^{-17}$	$9.69{\cdot}10^{-13}$

* CASSCF calculation was carried out by completing a rotation of the active space

** SCF in the F12-level calculations fails to converge. OH H-abstraction is a minor pathway for other cresols [2].

Initializing the restricted Hartree-Fock wavefunctions for the F12 failed to converge for our calculation for ortho-cresol OH H-abstraction. In addition to this, there is a substantial change in the barrier of around 7-8 kcal/mol for the OH-abstraction channel for the other two cresol isomers at the CCSD(T)-F12-level. This indicates that the known problems with the CCSD(T)-F12 calculation H-abstraction from -OH and -OOH groups persist to this system [2]. To assess the uncertainties, rates were also calculated at the ωB97X-D/aug-cc-pVTZ level of theory (denoted ωB97-level). The ωB97-level values in the corresponding order are: ortho-cresol: $7.38\cdot 10^{-12}$, $1.45 \cdot 10^{-10}$, $4.22 \cdot 10^{-13}$, $2.56 \cdot 10^{-12}$, $8.14 \cdot 10^{-13}$, $2.10 \cdot 10^{-11}$, $6.95 \cdot 10^{-12}$ and $3.26 \cdot 10^{-11}\ cm^3\ molecule^{-1}\ s^{-1}$, meta-cresol: $8.82 \cdot 10^{-13}$, $1.34 \cdot 10^{-9}$, $9.70 \cdot 10^{-13}$, $7.12 \cdot 10^{-11}$, $1.79 \cdot 10^{-13}$,$1.47 \cdot 10^{-9}$, $2.28 \cdot 10^{-11}$ and $5.54 \cdot 10^{-11}\ cm^3\ molecule^{-1}\ s^{-1}$ para-cresol: $8.17 \cdot 10^{-13}$, $1.23 \cdot 10^{-10}$, $8.58 \cdot 10^{-13}$, $1.04 \cdot 10^{-12}$, $4.16 \cdot 10^{-12}$ and $7.49 \cdot 10^{-11}\ cm^3\ molecule^{-1}\ s^{-1}$. While the main OH-addition pathways are still the same at the ωB97-level, the role of OH-abstraction pathway becomes relevant. However, the DFT rate coefficients have an uncertainty of a 100 compared to the uncertainty of a factor of 10 for the F12-level [2] making them inherently more unreliable. These uncertainties regarding phenolic H-abstraction don't affect our analysis regarding HOM formation, as the short timescale flow tube reactor experiments discussed in the section S19 as well as the main manuscript show HOMs result from OH-addition. Additionally, OH-abstraction is not a major pathway for ortho-cresol based on previous literature [4]. This is agreement with experimental works for phenol for which phenolic H-abstraction by OH is a minor pathway [11].

The measured OH reaction rate coefficients are: 3.41 - $4.90 \cdot 10^{-11}\ cm^3\ molecule^{-1}\ s^{-1}$ for ortho-cresol [17,18,19,20], 5.2 - $6.7 \cdot 10^{-11}\ cm^3\ molecule^{-1}\ s^{-1}$ for meta-cresol [17,18,19] and 4.8 - $5.2\cdot 10^{-11}\ cm^3\ molecule^{-1}\ s^{-1}$ for para-cresol [17,18,19]. The calculated total bimolecular rate coefficients in Table S1 are slower by an order-of-magnitude compared to the measurements. This is expected as computed absolute rate coefficients are known to be unreliable in literature for OH-addition/abstraction in aromatic systems, but the branching ratios are more reliable. [3]. For this reason, the branching ratios Γ are calculated using equation

$$\Gamma = \frac{k_{path}}{k_{total}} \cdot 100\%, \qquad (2)$$

and are presented in Table S2.

Table S2: Branching ratios (%) for OH-addition and H-abstraction at T=298K using bimolecular lowest conformer transition state theory at F12 level of theory.

cresol	1	2	3	4	5	6	CH_3 abs	OH-abs*
ortho	5.92	66.55	0.39	1.45	0.76	20.27	4.67	**
meta	0.05	28.38	0.06	1.88	0.02	69.26	0.35	0.00
para	1.11	92.80	1.57	2.05	-	-	2.46	0.01

* CASSCF calculation was carried out by completing a rotation of the active space

** SCF in the F12-level calculations fails to converge. OH H-abstraction seems to be a minor pathway for other cresols [2].

Our calculations are in agreement with previous studies. Wu et al. calculated branching ratios for ortho-cresol, and our results show good agreement with their results [4]. Their values at T=298K in corresponding order are 5.39, 55.53, 0.40, 1.42, 0.62, 27.68, 5.19 and 3.8%, indicating that OH-abstraction is a minor pathway.

Olariu et al [5] conducted experiments with the cresol isomers and OH. They measured a yield of 73.4 ± 14.6 % for 1,2-Dihydroxy-3-methylbenzene. This must form as result of OH-addition to position 2 for ortho-cresol, implying that this is indeed the major pathway, in agreement with our calculations. For meta-cresol, we are not aware of any computational works that calculate the rate coefficients or branching ratios. Olariu measured a yield of 68.67 ± 13.4 % for 1,2-Dihydroxy-3-methylbenzene, indicating that the position 6 addition is the major pathway with agreement with our calculations. A yield of 9.7 ± 2.7 % was assigned to 1,2-Dihydroxy-4-methylbenzene corresponding to the position 2 addition, in reasonable agreement with the calculation. For para-cresol, a yield of 64.1 ± 11.3% was measured for 1,2-Dihydroxy-4-methylbenzene, corresponding to position 2 addition being the major pathway in agreement with our mechanism. The experiments were conducted at 298K with NOx present. This will affect the results, but this should still give information about the major pathways for the OH-additions so comparisons can be made.

After OH-addition, the reverse reaction is also possible. To assess this, the stability of the OH-adducts is determined by calculating their energy with respect to the separated reactants. The addition to the OH carbon and to its ortho-positions (positions 1,2 and 6) are the most stable. For para-cresol, the geminal diol (position 1) addition is the most stable. This indicates that the reverse reactions for these positions are slow and unlikely to compete with O_2-addition reactions. The calculated zero-point corrected energies of the OH-adducts with respect to the free products can be seen in Table S3.

Table S3: ZPE-corrected electronic energy well of the OH-adducts with respect to the free products in kcal/mol

cresol	1	2	3	4	5	6
ortho	-19.7	-20.1	-16.4	-18.0	-18.0	-20.6
meta	-20.9	-19.7	-16.9	-17.0	-16.5	-21.1
para	-20.8	-20.6	-18.2	-19.4		

S2: BPRs and molecular rearrangement

Bicyclic peroxy radicals (BPRs) are important intermediates in the OH initiated autoxidation of many aromatics. In this section we are interested in the molecular rearrangement rates of the BPRs formed from OH-addition to the cresol isomers as this can result in highly oxygenated molecules that contribute to aerosol formation [7]. The formation of BPRs for different aromatics and different OH-addition sites follow identical steps due to the similarity of the structures [7, 8, 12, 13]. The steps are later outlined in more detail for the geminal diol additions in section S3.

Molecular rearrangement involves the breaking of the BPR's endoperoxide bridge and one of the carbon-carbon bonds adjacent to the OH, followed by a H-shift. There are two possible pathways for molecular rearrangement, and these are shown for one BPR conformer in Fig. S2, along with the notations used. For example, m4 denotes BPRs formed from OH-addition to position 4 to meta-cresol. O_2 can add to either of the meta-positions relative to the OH-addition site (positions 2 and 6 in Fig. S1), resulting in asymmetric structures. These are denoted m4-L and m4-R of which two transition states are presented for the former in Fig. S2. The notation

"-L" and "-R" denotes the location of the peroxy radical group with respect to the perspective shown in the figure; the endoperoxide bridge is at the front with respect to the plane coinciding with the carbon ring and the OH-attack location is at the top of the molecule. The broken endoperoxide bridge is seen in the transition states in Fig. S2, the carbon bond breaking is shown as a dotted line, and the H-shift is illustrated with an arrow. The direction of the C-C bond breaking is denoted with additional parenthesis notation (L/R) following similar logic. The L(R) and R(L) notation corresponds to C_1 and L(L) and R(R) correspond to C_2 notation used in the main manuscript.

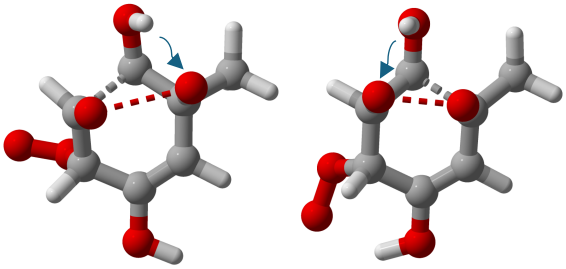

m4-L(L) m4-L(R)

Fig. S2: Example BPRs showing the molecular rearrangement transition states.

Molecular rearrangement rates are presented in Table S4. Rate coefficients that are potentially competitive under atmospheric conditions (>1· 10^{-3} s^{-1}) are bolded and ipso-position carbons are underscored. The notations used are explained above, with the two values in the table corresponding to the left/and right opening direction in that order. For example, for m4-L(L) and m4-L(R) the rate coefficients are $3.52 \cdot 10^{-6}$ and $3.36 \cdot 10^{-6}$ s^{-1}, respectively. The rate coefficients were calculated at the F12-level of theory using lowest conformer transition state theory (LC-TST). Tunneling is ignored as the imaginary frequencies associated are in the order of 500 cm^{-1} or less amounting to very small corrections for the rate coefficient. LC-TST is deemed sufficient, as there are very few transition states corresponding to molecular rearrangement, typically only one in the 2 kcal/mol range used as a cutoff for the conformer sampling. More reactants are possible within the cutoff range. This means that single conformer TST overestimates the rate coefficients compared to the multi-conformer TST (MC-TST). The current analysis is done to rule out uncompetitive molecular rearrangement pathways, and therefore LC-TST is deemed sufficient.

The notation "x" means that the transition state was not found. In these cases, the structure optimizes to the transition state for which the value is shown regardless of the constraints used. This is the case for ortho-position addition (X = 2 or 6) as molecular rearrangement this way would lead to an unstable geminal diol intermediate.

Table S4: Molecular rearrangement rate coefficients (s^{-1}) for all possible cresol BPRs. LC-TST is used without tunneling at F12-level of theory. X denotes OH-addition site, L/R denotes location of O_2-addition site. The two values correspond to the two possible ways molecular rearrangement can take place, i.e. which C-C bond breaks. This is denoted as (L) or (R), see Fig. S2.

X	1	2	3	4	5	6

mX-L (L/R)	**$\underline{1.75 \cdot 10^2}$** / **$\underline{6.89 \cdot 10^4}$**	**$1.49 \cdot 10^{-3}$**/ x	$1.68 \cdot 10^{-4}$/ **$3.04 \cdot 10^{-2}$**	$3.52 \cdot 10^{-6}$/ $3.36 \cdot 10^{-6}$	**$\underline{1.12 \cdot 10^{-1}}$**/ **$\underline{1.53 \cdot 10^{-3}}$**	x/ $8.70 \cdot 10^{-8}$
mX-R (L/R)	**$\underline{1.76 \cdot 10^4}$**/ **$\underline{3.91 \cdot 10^2}$**	$7.77 \cdot 10^{-5}$/ x	$2.35 \cdot 10^{-4}$/ **$1.12 \cdot 10^{-3}$**	$2.14 \cdot 10^{-8}$/ $1.32 \cdot 10^{-5}$	**$\underline{1.56}$**/ **$\underline{1.15 \cdot 10^{-1}}$**	x/ $5.02 \cdot 10^{-7}$
oX-L (L/R)	**$\underline{5.35 \cdot 10^3}$**/ **$\underline{8.65 \cdot 10^{-1}}$**	**$3.09 \cdot 10^{-3}$**/ x	$1.35 \cdot 10^{-5}$/ $7.48 \cdot 10^{-6}$	**$3.72 \cdot 10^{-3}$**/ $5.50 \cdot 10^{-4}$	$1.12 \cdot 10^{-5}$/ $1.02 \cdot 10^{-5}$	$\underline{x}$/ **$\underline{7.10 \cdot 10^{-3}}$**
oX-R (L/R)	**$\underline{2.76 \cdot 10^2}$**/ **$\underline{6.51 \cdot 10^{-2}}$**	$1.31 \cdot 10^{-5}$/ x	**$9.14 \cdot 10^{-3}$**/ $4.56 \cdot 10^{-5}$**	$1.90 \cdot 10^{-4}$/ $6.63 \cdot 10^{-5}$**	$3.81 \cdot 10^{-6}$/ $5.85 \cdot 10^{-11}$**	$\underline{x}$/ **$\underline{5.28 \cdot 10^2}$**
pX-L (L/R)	**$\underline{1.20 \cdot 10^2}$**/ **$\underline{5.93 \cdot 10^3}$**	**$1.46 \cdot 10^{-3}$**/ x	$6.28 \cdot 10^{-8}$/ $2.01 \cdot 10^{-7}$**	**$\underline{8.38 \cdot 10^{-2}}$**/ **$\underline{8.76 \cdot 10^{-2}}$**	-/ -	-/ -
pX-R (L/R)	-/ -	**$4.63 \cdot 10^{-2}$**/ x	$8.66 \cdot 10^{-9}$/ $1.18 \cdot 10^{-5}$	-/ -	-/ -	-/ -

x = transition state not found, optimization leads to the transition state opening to the other side.

** = ωB97-level of theory is used.

- = Structure already considered due to symmetry

We see that the molecular rearrangement of geminal diol BPRs, corresponding to position 1 addition, is extraordinarily fast for all the cresols. This is analogous to the non-oxygenated aromatics for which the methyl ipso-position addition yields the highest molecular rearrangement rate coefficients [7], but the molecular rearrangement of these geminal diol BPRs is much faster ($1 \cdot 10^2 - 1 \cdot 10^4\ s^{-1} >> 1 s^{-1}$). The transition state is stabilized by the presence of the $ROO \cdot -HO$ interaction (See Fig. 3 of main manuscript) that lowers the reaction barrier by roughly 3 kcal/mol. Transition states where this interaction is present were found only for one of the opening directions, meaning that the transitions that were found lack this interaction and thus have higher barriers. For para- and meta-cresol the C_1 (L(R) and R(L)) transition states have the interaction, whereas for ortho-cresol the L(L) and R(L) transition states have this stabilizing interaction.

When it comes to the viability of molecular rearrangement under atmospheric conditions, pathways other than the position 1 (geminal diol) addition are expected to be limited. Firstly, the LC-TST rate coefficients are overestimating the true rate coefficients, meaning that the likely fate of many of the non-geminal diol BPRs is to undergo bimolecular sink reactions with e.g. NO under atmospheric conditions. Secondly, the main fate of the pathways resulting from OH-addition to the non-substituted carbon is H-abstraction leading to the formation of dihydroxytoluenes seen in large yields experimentally by Olariu et al [5]. Thus, limited direct autoxidation to HOM formation is expected from these pathways. The potential pathway, meaning m1, m5, o1, o6, p1 and p4, are considered in more detail in sections S3-S13 to determine their possible contribution to HOM yields.

S3: Ortho-cresol: Initial steps in o1 (geminal diol) oxidation (6% yield)

OH-addition to the C(OH) substituted carbon (position 1) leads to a geminal diol intermediate. The OH-adduct exists in an energy well of -19.7 kcal/mol and has an OH loss rate coefficient of $1.8 \cdot 10^{-3}\ s^{-1}$ at the F12-level of single conformer TST. Geminal diols in liquid phase are often unstable, favoring H_2O loss [16]. The transition state for H_2O loss directly from the OH-adduct was not found despite numerous attempts, with every TS optimization collapsing to the transition state for OH H-abstraction from C-OH. A relaxed scan was performed varying the H-OH distance at B3LYP/6-31+G(d) level of theory, henceforth denoted as B3LYP. The highest point in this structure before the H_2O-loss was around 30 kcal/mol higher in energy compared to the adduct. This is seen in Fig. S3. Transition states for H_2O loss at every other point of the

BPR formation process were found and the barriers are similarly high with values of around 40 kcal/mol at the same level of theory. H_2O-loss is therefore not favored and O_2-addition is the main pathway.

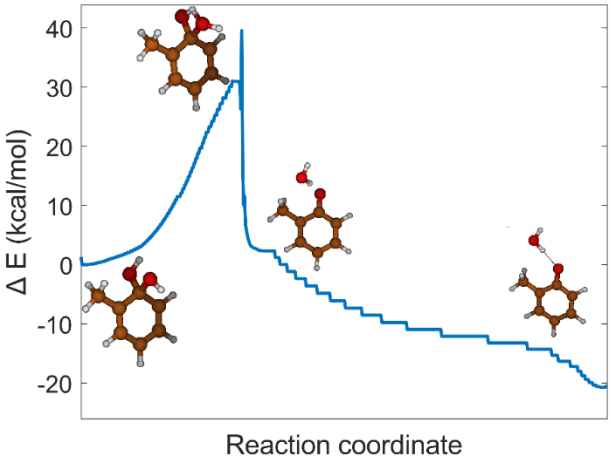

Fig. S3: Scan for H_2O loss. The H-OH distance was varied by performing a relaxed scan and the resulting electronic energies at B3LYP level-of-theory are presented in the figure.

The oxidation pathway of o1 is illustrated in Fig. S4. Unlike many of the possible OH-adducts, the geminal diol is symmetric with respect to the plane of the ring, and thus the syn/anti O_2-additions are identical. Like with all ipso-positions, radical termination via H-abstraction by O_2 is not possible and thus O_2-addition is the main pathway. This can happen at 3 different locations. For the non-oxygenated aromatics, para-addition reaches an equilibrium between addition and decomposition as further reactions are not atmospherically competitive [14]. For phenolic compounds, however, the additional OH group can potentially provide atmospherically competitive pathways that are not present for the non-oxygenated aromatics. For O_2-addition to the para-position relative to the initial OH-addition, the H-shift from the OH group was considered and found to be slow, see Table S5. Further autoxidation is possible via O_2-addition to ortho-position, as this can result in BPR endoperoxide bridge formation due to the stabilizing interaction of the OH group.

O_2-addition to the methyl substituted carbon is favored with a yield of roughly 95% based on the rate coefficients. This leads to the formation of a peroxy radical. The main fate of these aromatic peroxy radicals in general is ring closure, with an endoperoxide bridge over the OH (Endo-R, Endo-L) being most competitive [7, 8, 12, 13]. However, this pathway has a competing reaction to BPR formation, the OH H-shift denoted OH-L/R. The reaction has a higher barrier of around 16.7 kcal/mol compared to the 14.0 kcal/mol barrier for endocyclization, but the reaction is driven by tunneling. This H-shift results in a ring-broken carboxylic acid, with ring opening happening in the IRC calculation. This carboxylic acid could have atmospheric relevance due to the carboxylic acid functionality lowering its volatility. Accurate branching ratios between the OH H-shifts and endocyclization are difficult to determine. As described previously in section S1, CCSD(T) calculations of OH H-shifts are susceptible to artefact solutions. Wavefunction stability checks were carried out to ensure that the initial reference Hartree-Fock wave function for the CCSD(T) calculation converged to the correct lowest energy state. The final F12 corrected barrier for the OH H-shift is within 1

kcal/mol of the DFT barrier, which indicates reliable CCSD(T) energies. In addition to the unreliability of the CCSD(T) correction, tunneling might be overestimated by Eckart tunneling due to the concerted nature of the reaction. This is considered in section S3.1. The branching ratios for endocyclization in the OH-L pathway range from 20 % at 87 % depending on the method and the tunneling factor (See section S3.1).

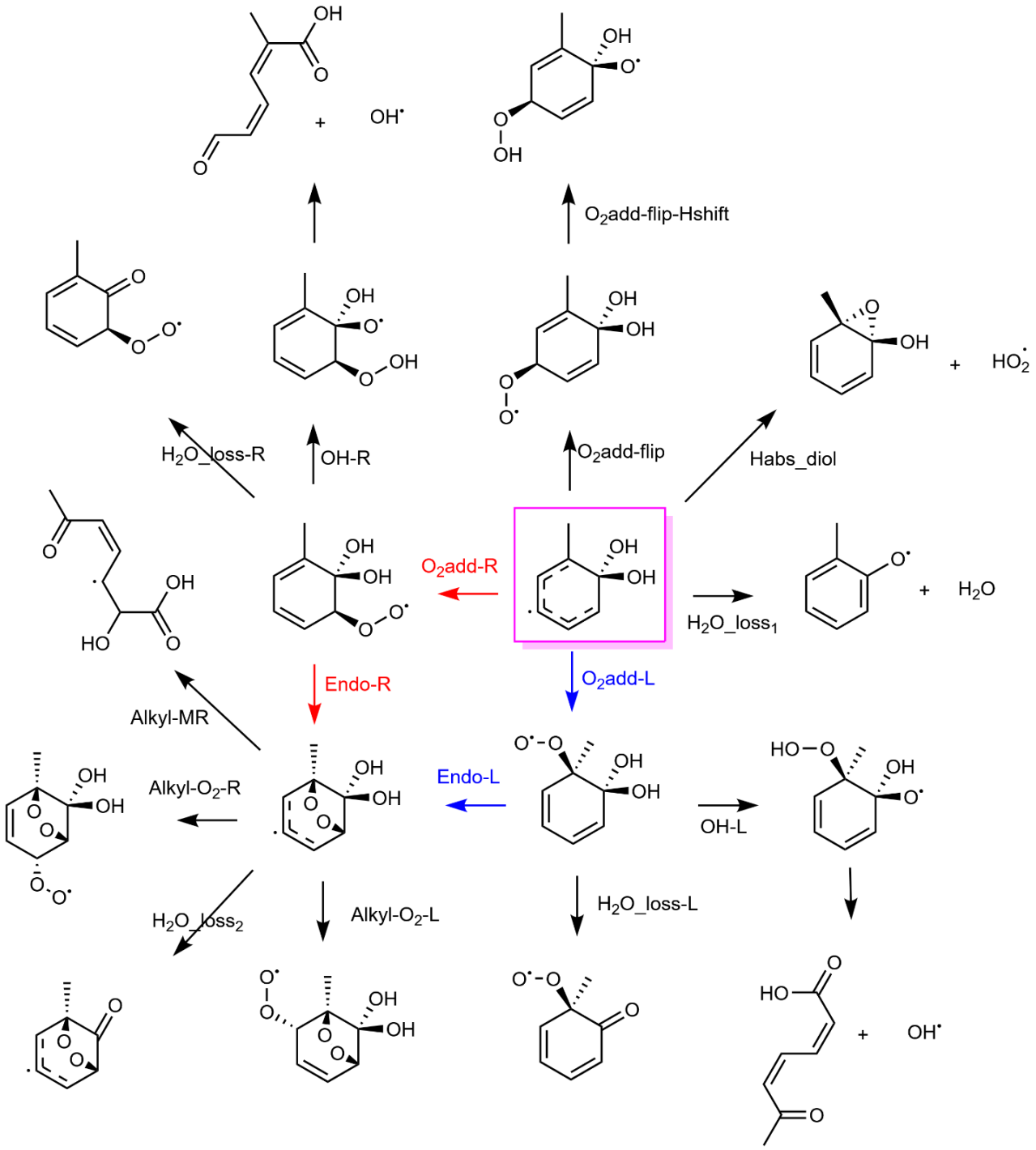

Fig. S4: Formation scheme for o1 BPR formation. The main fate of the ortho-cresol geminal diol OH-adduct is to undergo endocyclization. The other reactions are presented in the figure but are found to be slow, see table S5. Out of the two possible endocyclization pathways, addition to the C(CH_3) carbon (blue pathway) has a branching ratio of 95% based on the

thermalized rate coefficients. Endocyclization competes with a terminating H-shift, but the endocyclization has a branching ratio of 20% - 87% (See section S3.1). The main fate of the alkyl adduct is BPR formation.

Table S5: LC-TST rates at T = 298.15K unless otherwise stated. Mostly no tunneling corrections except for H-shifts.

Reaction	Rate (s^{-1})
H2O_loss1**	No TS found, highest point of relaxed scan has a barrier of 40kcal/mol with the constrained optimization of the highest structure being 34 kcal/mol
Habs_diol**	$6.6 \cdot 10^{-11}$
O2add-flip [b]	12.2
O2add-flip-Hshift*	$1.4 \cdot 10^{-14}$ (no tunneling, freq. ~ 3074 cm^{-1})
O2add-L [b]	$5.51 \cdot 10^{2}$
O2add-R [b]	30.6
OH-L [a] (MC-TST + eckhart tunneling)	23.4 (F12) / 228 (wb97)
OH-R [a] (MC-TST + eckhart tunneling)	19 (F12) / 93.2 (wb97)
H2O_loss-L**	$1.05 \cdot 10^{-17}$
H2O_loss-R**	$1.67 \cdot 10^{-16}$
Endo-L (MC-TST, no tunneling, freq = -579)	59.7
Endo-R (MC-TST, no tunneling, freq = -551)	4.27

* ωB97, **(b3lyp)

[a] the barriers are very high and the rate by itself is less than $1s^{-1}$, but the reaction is driven by tunneling. Tunneling from IRC endpoints at ωB97-level

[b] Pseudo-unimolecular rates calculated for O_2 concentration of $5 \cdot 10^{18}$ #/cm^3

Following endocyclization, an alkyl radical is formed. The alkyl radical can either undergo unimolecular reactions or undergo O_2-addition to form the geminal diol BPR. Epoxide formation could be possible at the alkyl stage, but no transition state was found for this, with the TS relaxing to the structure for the molecular rearrangement instead. Epoxide transition states were found for other OH-addition (o2 and o6) sites, but they were found to be too slow to compete with O_2-addition (0.35 s^{-1} and 0.08 s^{-1} for o2 and o6 respectively). As shown previously for toluene and benzene, epoxide formation is not competitive with O_2-addition reactions under atmospheric conditions [7,8], and thus are unlikely to contribute here either [8]. The alkyl radical can undergo both possible molecular rearrangement reactions (C_1 or C_2) with comparable rates, as the stabilizing $ROO \cdot -OH$ interaction is not present. Breaking the C(CH_3)-C(OH) bond at the alkyl stage has a lower barrier, and the subsequent chemistry would likely be identical to that of the molecular rearrangement of the BPR. While the molecular rearrangement rate coefficients of the alkyl radicals are fast, they are orders of magnitude slower than O_2-addition reactions (see Table S6). The O_2 anti-addition (relative to the endoperoxide bridge) is favored based on previous works on aromatics (32 times more likely for benzene derived bicyclic alkyl radical according to reference: [8]).

Table S6: Rates at LC-TST, no tunneling unless otherwise stated

Reaction	Rate (s^{-1})
Alkyl-O2-R*	333.6
Alkyl-O2-L*	113.4
Alkyl-MR (molecular rearrangement) 1 (L)	7.3

Alkyl-MR (molecular rearrangement) 2 (R)	3.9
H2O_loss2	$3.36 \cdot 10^{-18}$ **

*Pseudo-unimolecular rates calculated for O_2 concentration of $5{\cdot}10^{18}$ $\#/cm^3$
**(B3LYP)

S3.1: Overestimation of tunneling factors in complex concerted reactions

When using Eckart tunneling with the high imaginary frequencies associated with H-shift reactions, one assumes that the potential energy associated movement of the hydrogen atom and the subsequent minor relaxation is sufficiently described by the shape of the Eckart potential. However, if the H-shift is followed by a ring-breaking reaction, the subsequent relaxation of the structure leads to a significantly deeper product well for the overall reaction. Using this product well for Eckart tunneling assumes an incorrect shape for the potential energy surface. Fig. S5 a) represents (electronic) potential energy as a function of the IRC points. As these points are calculated using gradient descent method, the plotted visual shape of the potential depends on the number of optimization steps. A more physically realistic potential energy surface is obtained by plotting the energy as a function of a physical quantity, in this case the distance travelled by the hydrogen. This is illustrated in Fig. S5 b). Potential energy is plotted as a function of the change in distance between the H of the OH group and the O of the peroxy radical. Once an equilibrium distance is reached, corresponding to a total change in distance of roughly 0.9Å, the rest of the potential energy is due to the carbon ring-breaking. Thus, using the potential well depth of 5-10 kcal/mol might be more accurate for the tunneling correction. Using these wells for the Eckart tunneling, the tunneling correction drops from 30.5 at the ω97 level (28.9 at F12-level) when using the final product well down to 9.4 (11.7 at F12) and 17.5 (19.8 at F12) for +10 and +5 kcal/mol wells, respectively. These values increase the endocyclization branching ratios to 30% and 45% at ωb97-level and 80 and 87% at F12-level, respectively.

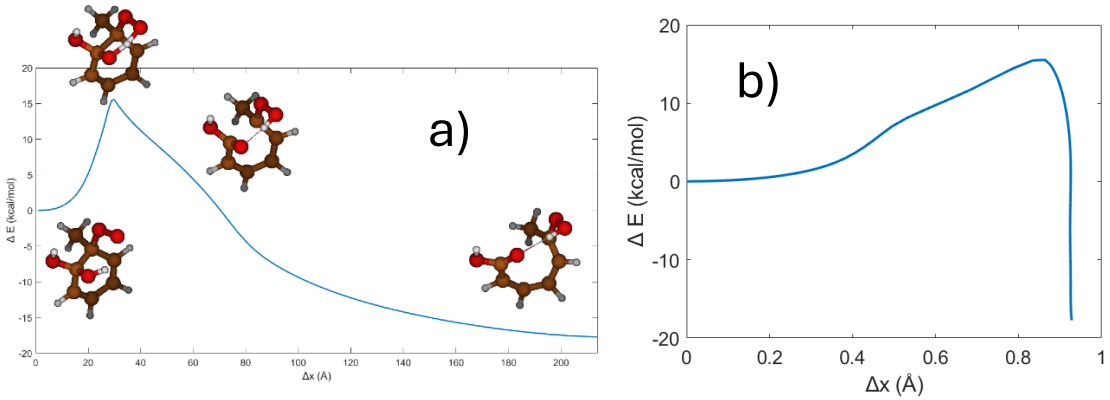

Fig. S5: Energy surface for Eckart tunneling correction. a) Potential energy surface based on the intrinsic reaction coordinate (IRC) for the H-shift reaction. b) Potential energy as a function of the change in the H-O distance of the hydrogen shift.

S4: Reactions competing with molecular rearrangement

Once the BPR forms, it may undergo unimolecular H-shifts. These were considered at the B3LYP-level of theory and found to be slow. The OH H-shift to form a carbonyl + H_2O, which is not present for non-oxygenated aromatics was calculated at the ωb97 level-of-theory and

found to also be slow. Therefore, molecular rearrangement is the only competitive unimolecular pathway for the geminal diol BPRs.

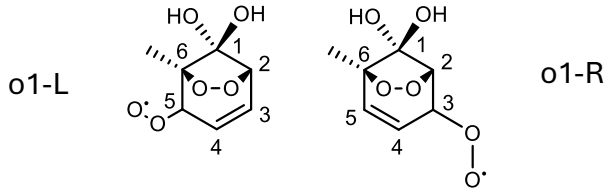

Fig. S6: Notations used for the two possible geminal diol BPRs from ortho-cresol. All of the H-shift were found to be slow, see table S7

Table S7: Rate coefficients for the H-shifts and H_2O loss at the BPR stage (s^{-1}), B3LYP level of theory, T=298.15

	1 (OH)	2	3	4	5	6 (CH_3)	H2O loss
o1-BPR-L	$4.42 \cdot 10^{-3}$*	$6.0 \cdot 10^{-64}$	$2.8 \cdot 10^{-38}$	$1.5 \cdot 10^{-23}$	$3.4 \cdot 10^{-16}$	$1.7 \cdot 10^{-13}$	$6.1 \cdot 10^{-19}$
o1-BPR-R	$4.02 \cdot 10^{-7}$* (No tunneling)	$3.2 \cdot 10^{-13}$	-	-	-	-	$2.9 \cdot 10^{-19}$

*LC-TST, wb97

S5: Subsequent chemistry for o1

Molecular rearrangement leads to ring-opened peroxy radicals that have a significant amount (~65 kcal/mol) of excess energy. This excess energy can drive reactions that would otherwise not be favoured for thermalized molecules [7,15]. RRKM-ME simulations using MESMER [10] were perfomed and the branching ratios are given in Fig. S7 and Fig. 4 in the main manuscript. The products in the simulation are the optimized endpoints of the IRC-calculation and these are treated as sinks. As was discussed in section S1, initializing the Hartree-Fock wavefunction for the CCSD(T)-F12 calculation is known to not always find the lowest energy configuration when dealing with H-shift reaction from -OH and -OOH groups [2]. For this reason, ωb97 level-of-theory is used for these reaction types. This results in uncertainties of around 100 for the rate coefficients [2].

The fate of the o1-BPR-L has been discussed in the main manuscript, except for the C_1 pathway. The proposed oxidation mechanism is illustrated in Fig. S7.

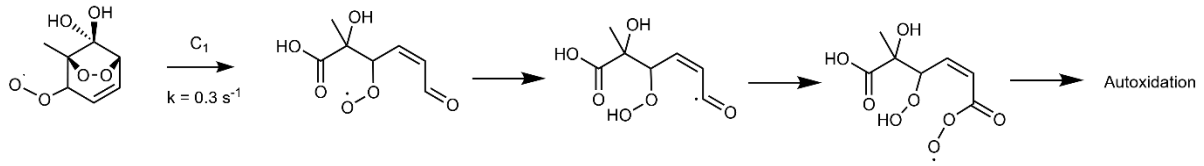

Fig. S7: Proposed oxidation mechanism for the o1-L C_1 pathway. The main oxidation is likely initiated by 1,6 aldehydic H-shift.

For the o1-BPR-R case, there is uncertainty in the OH H-shift barriers at F12-level as has been previously discussed. Glyoxylic acid formation takes place via β-scission and the other pathway leads to closed-shell species via termination. Glyoxylic acid formation from cresol

oxidation has previously been observed in chamber experiments [21] and it was also detected in this work using Br^--CIMS (See section S21).

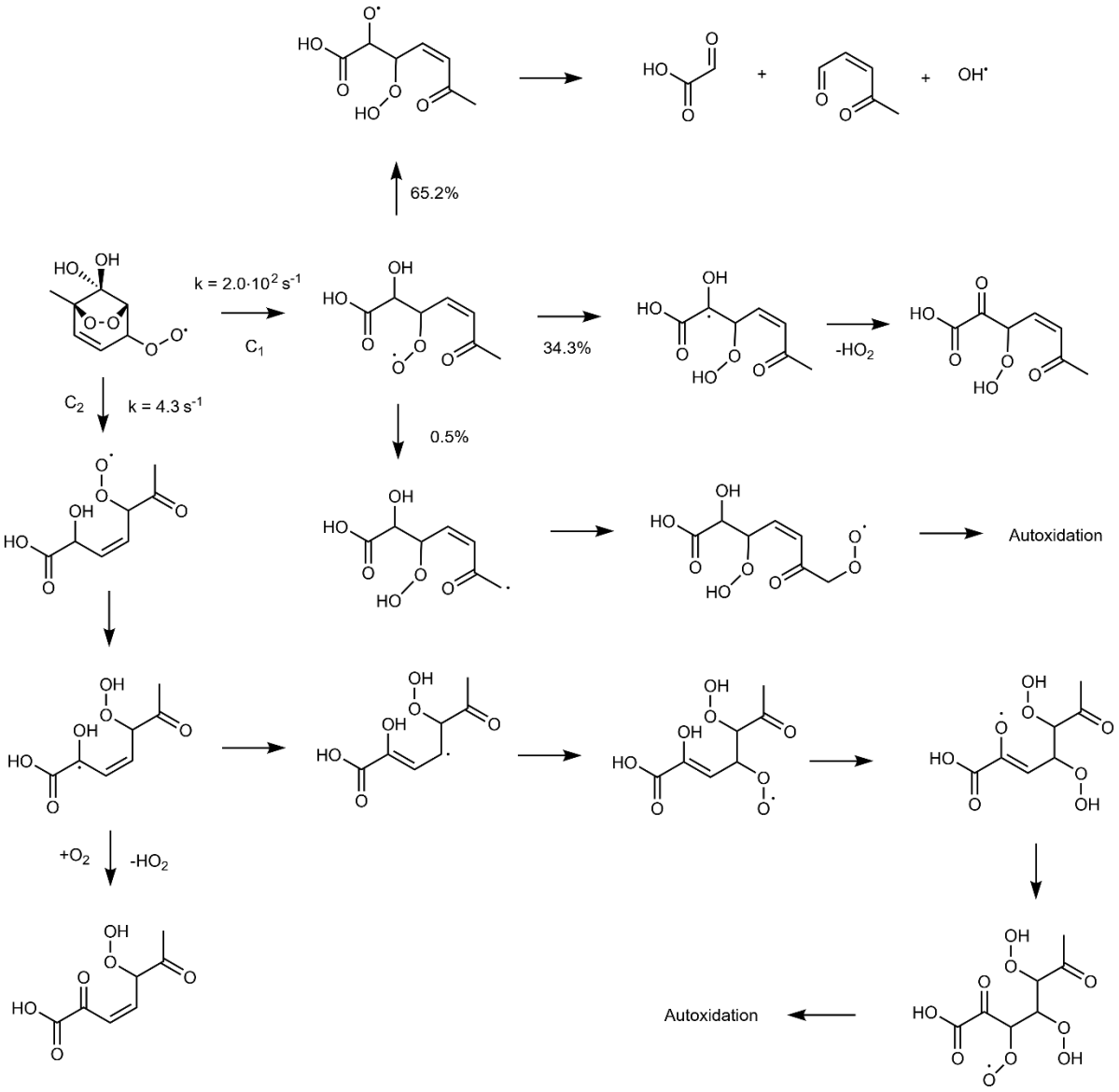

Fig. S8: Scheme for o1-R autoxidation. The other ortho-cresol BPR will lead to termination either via HO_2-loss or by fragmentation via β-scission. This leads to the formation of glyoxylic acid and OH recycling. The C_2-pathway likely leads to HOM starting with a 1,6 H-shift similar to Fig. 4 of the main manuscript.

S6: Ortho-cresol: Fate of the o6 (OH-addition to C(CH_3)-carbon) adduct (20% yield)

OH-addition to the methyl substituted carbon and the molecular rearrangement of the consequent BPR could potentially lead to HOM. Although the rate coefficients seen in Table S4 are much slower relative to the molecular rearrangement of geminal diol BPRs, the initial OH yield is significant. The BPR formation of the o6 adduct is presented in Table S8 and S9 and Figures S9 and S10, with pseudo-unimolecular rates being presented for the bimolecular

reactions. The main fate based on the rates is to undergo O_2-addition to the C(OH) leading to HO_2-loss. However, there are significant uncertainties in the calculated branching ratios as optimizing transition states for O_2-addition reactions to alkyl radicals using DFT methods is difficult. This can result in low-energy conformers being missed skewing the calculated branching ratio. This is supported by the fact that structures compatible with BPRs are detected experimentally. Note that the o6-BPRs are likely more prone to cluster with NO_3^- and consequently be measured by nitrate-CIMS compared to many other aromatics due to the presence two OH groups on adjacent carbon atoms. Based on the low molecular rearrangement rate coefficient, the BPRs are stable enough to accumulate in the experimental timescale but could contribute to HOM formation in pristine atmospheric conditions where they have longer lifetimes.

Table S8: Rate coefficients (s^{-1}) relating O6 BPR formation. Lowest conformer transition state theory at T=298.15 K at F12-level of theory unless otherwise stated.

	Rate coefficient (s^{-1})
O2add-R1*	$2.4 \cdot 10^5$
O2add-R2*	$9.9 \cdot 10^2$
O2add-L*	$1.4 \cdot 10^3$
OH-L*	$4.5 \cdot 10^{-4}$ (No tunneling)
Endo-L	$6.4 \cdot 10^3$
Endo-R	$4.2 \cdot 10^3$
OH-R_Anti**	$7.08 \cdot 10^8$ (No tunneling)

*Pseudo-unimolecular rates calculated for O_2 concentration of $5 \cdot 10^{18}$ #/cm^3
** ωB97

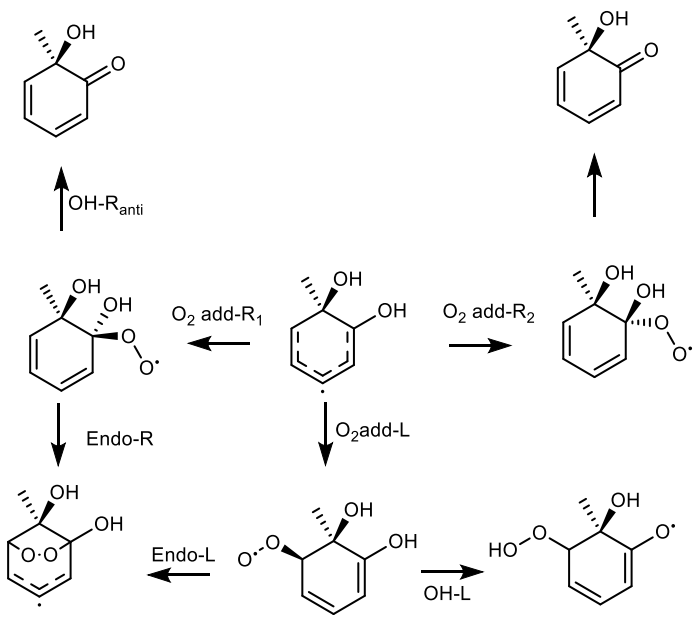

Fig. S9: Fate of o6 adduct. Based on the computed rates, O_2 addition to the C(OH) carbon is favored leading to termination via HO_2 loss. However, experimentally structures corresponding to BPRs are seen and thus some O_2-addition to the other carbon is expected to take place.

At this stage, there are two O_2-addition locations. The rates for these are given in Table S9, with the branching ratio based on these being roughly 63% of the O_2 adding to form o6-L and 37% to form o6-R.

Table S9: Rate coefficients (s^{-1}) for BPR formation. Lowest conformer transition state theory used at F12-level of theory unless otherwise stated. T=298.15K

Name	Rate coefficient (s^{-1})
Alkyl-O2-L	156.9
Alkyl-O2-R	92.3
1,5 H-shift	$5.54 \cdot 10^{-4}$

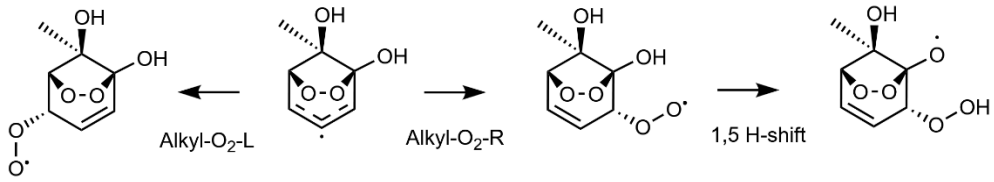

Fig. S10: o6-BPR-L formation from O6 alkyl radical. The formation of the BPR on the left is favored based on the rate coefficients.

S7: Subsequent chemistry for o6

The subsequent chemistry is shown in Fig. S11 and S12.

S7.1: o6-BPR-L

The molecular rearrangement rate is slow ($6.7 \cdot 10^{-3}\ s^{-1}$) and this pathway is thus unlikely to lead to HOM in our experimental conditions.

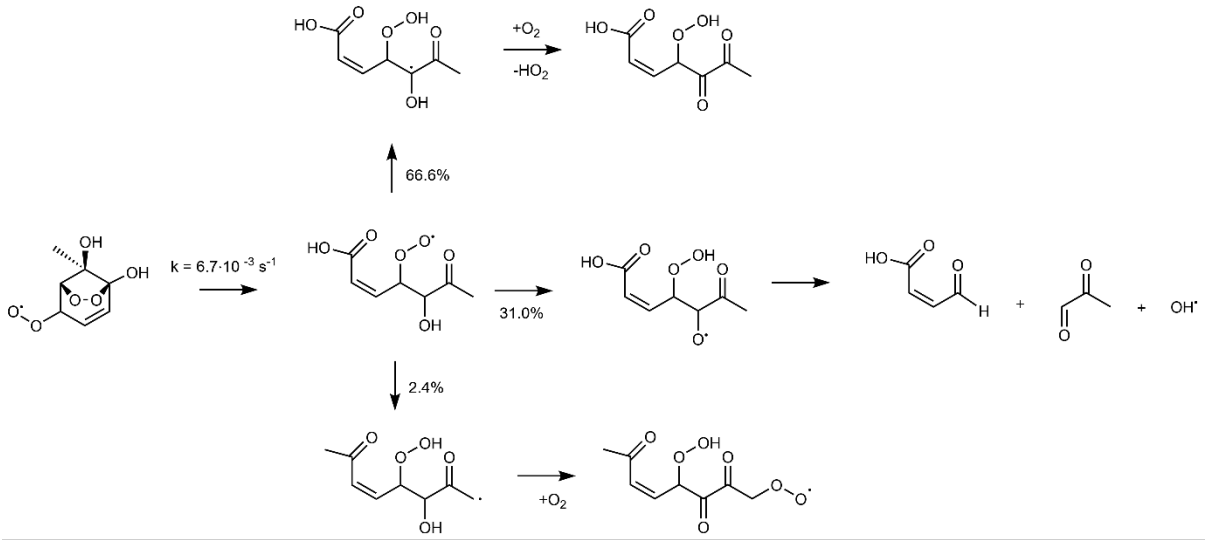

Fig. S11: o6-L autoxidation. The main fate of the autoxidation is termination via HO_2 loss or fragmentation to methyl glyoxal via β-scission, but some autoxidation can take place via H-shift from the methyl group. Note that an increase in methyl glyoxal signal wasn't detected in the Br^{-1}-CIMS spectrum as the concentration of cresol was increased.

S7.2: o6-BPR-R

This pathway has a rate of $7.3 \cdot 10^{-2}\ s^{-1}$ and is unlikely to contribute to HOM in our experiments. Despite the high OH-yield to the o6 pathway, BPR formation is limited by the factors considered in section S6. In addition, the main fate of this pathway is the OH H-shift that leads to termination by kicking out CO_2 along with OH recycling.

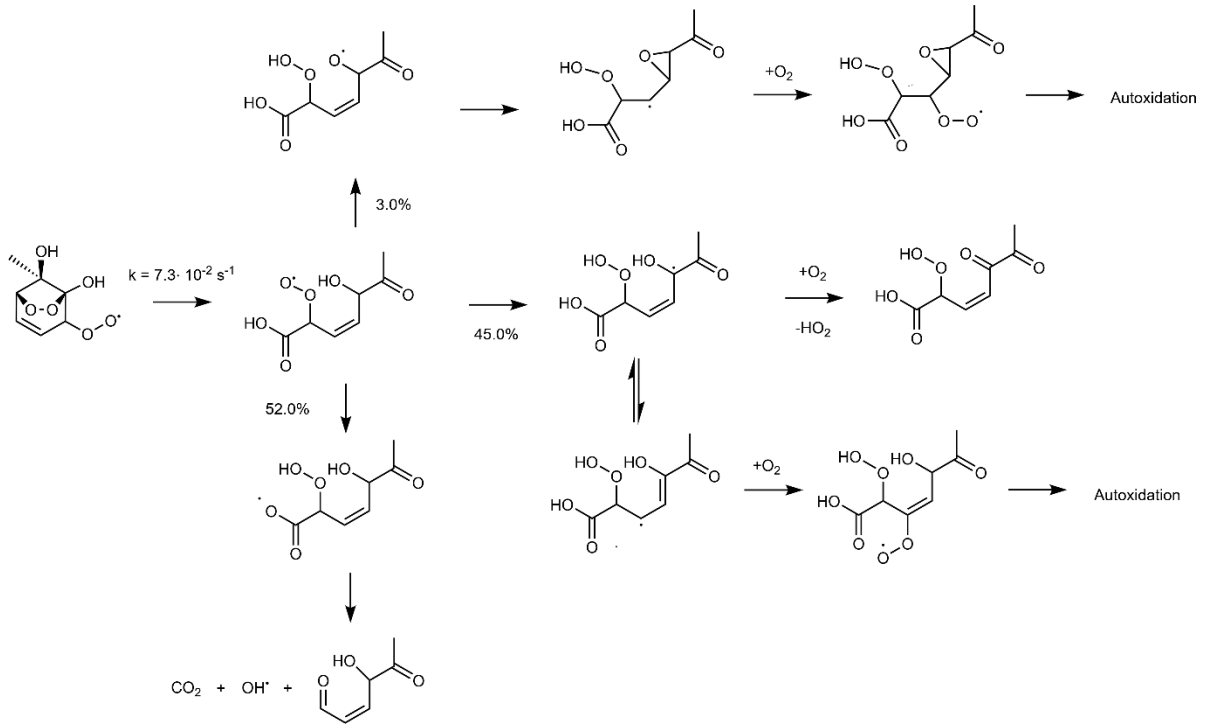

Fig. S12: o6-R autoxidation. The main fate of this pathway is CO_2 loss. Like other OH-related H-shifts, this transition state is subject to larger uncertainties as ωb97 level-of-theory is used. HOMs could form as a result of similar H-shifts as for the geminal diol pathway, but due to the relatively slow molecular rearrangement rates and small branching ratios indicate low HOM yields from this pathway.

S8: Para cresol geminal diol (p1) formation

The para-cresol geminal diol OH-adduct is stable based on Table S3. The geminal diol BPR formation should follow similar steps to o1. O_2 adds to the OH-adduct and the consequent peroxy radical can either do an H-shift and terminate or undergo endocyclization to form the alkyl radical. The terminating OH H-shift has a rate of 1.69 s^{-1} at F12-level and 7.73 s^{-1} at ωb97 level (MC-TST with tunneling), whereas the ring-closure has a rate of 0.23 s^{-1} (F12, MC-TST). This indicates that the termination is the major pathway, but some fraction goes on to form BPRs. Like ortho-cresol, the concerted nature of the H-shift reaction might lead to an over-estimation of the tunneling correction. Using the same potential energy wells (+5 and +10 kcal/mol) as in section S3.1 to calculate the tunneling corrections, the correction drops from 75.0 down to 23.4 and 43.5 for +10 and +5 kcal/mol respectively at the F12-level, and from 73.6 down to 20.1 and 39.1 respectively at the ωb97 level of theory. Using these values changes the branching ratios of BPR formation from 12% to 30% at F12-level of theory and 5% to 10% at the ωb97-level of theory.

S9: Subsequent chemistry

The C_1 and C_2 pathways have rate coefficients of $4.5 \cdot 10^3 s^{-1}$ and 84 s^{-1} respectively. The blue and green pathway lead to O_8 peroxy radicals via 1,6 aldehydic H-shift or 5-membered ring-formation. These compounds can potentially oxidize further. The C_2 pathway (red) can lead efficiently to O_{12}-compounds. Note, however, that these reactions are inferred from the available H-shift reactions and not explicitly calculated.

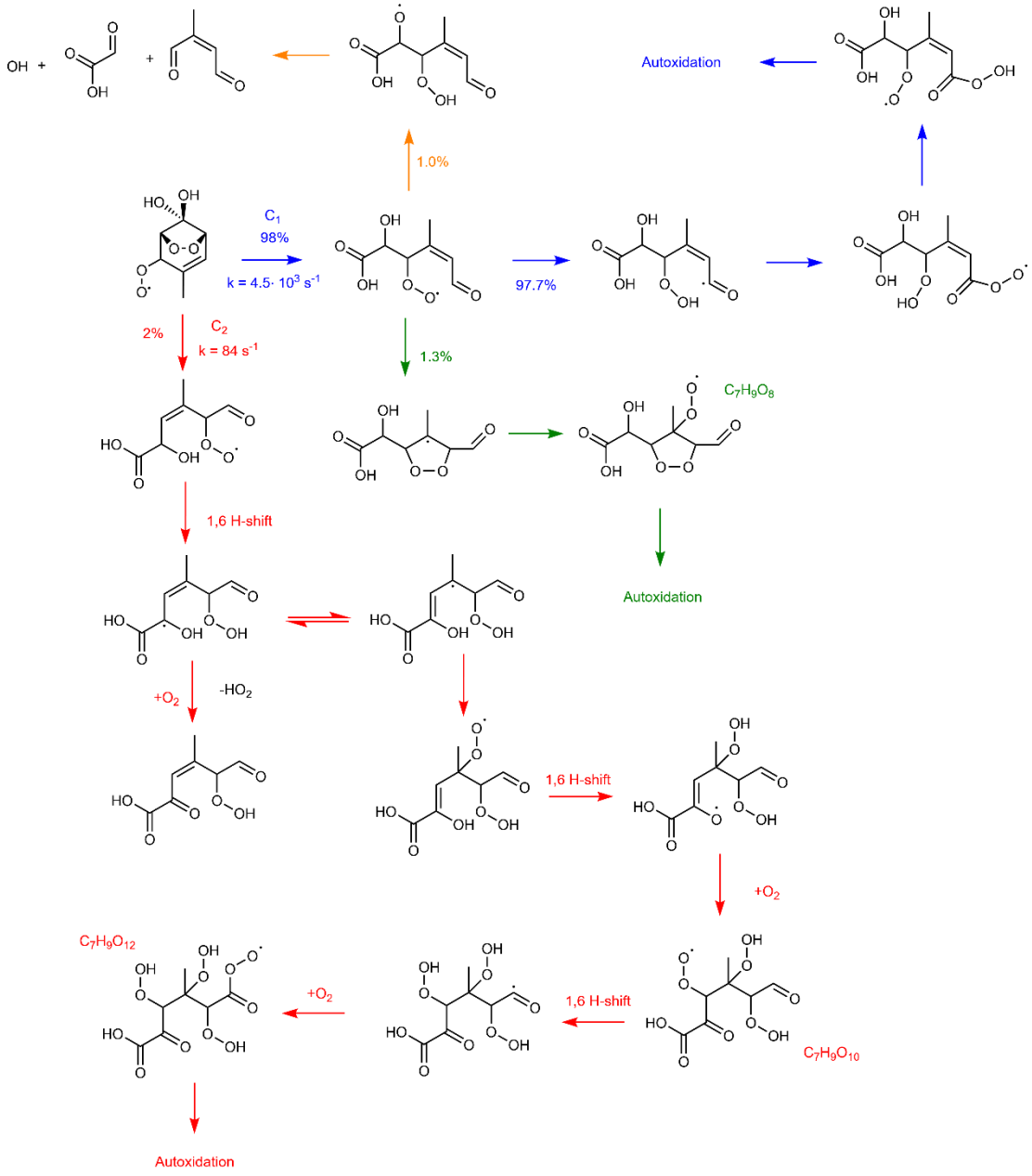

Fig. 13: Para-cresol geminal diol autoxidation. The C_1-pathway can lead to the the formation of O_8-compounds via 1,6 aldehydic H-shift or 5-membered ring formation and the C_2-pathway can lead to O_{10} and O_{12}-compounds via 1,6 H-shifts.

S10: Para-cresol methyl-ipso (p4) formation

BPRs formed from OH-addition to the methyl substituted carbon have molecular rearrangement rates that are relatively slow but could contribute to HOM formation in pristine conditions. The O_2-addition sites and HO_2-loss barriers determine the fate of the p4 OH-adduct, with the computed rate coefficients indicating that O_2-addition to the OH-substituted carbon is highly favored. However, like o6, it is likely that some BPR formation takes place. This involves O_2 addition to the ortho-position, and due to the similarity of the structures the subsequent ring-closure likely follows similar steps to the previously discussed steps for ortho-cresol. Additionally, due to the similarity of the p4 BPR and toluene ipso-BPR, we can also refer to the supplementary material of [7] where the toluene ipso-BPR formation is discussed. Due to the placement of the OH groups, it is likely that only one group clusters with NO_3^-, leading to weak clusters and consequently the p4 BPRs are less sensitively detected by nitrate-CIMS compared to o6. The computed rate coefficients for O_2-addition are presented in Table S10 and the reactions are illustrated in Fig. S15.

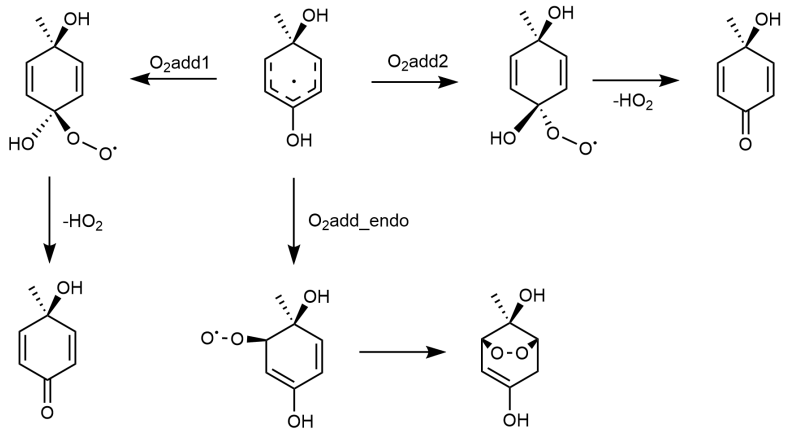

Fig. S15: The reaction mechanism of p4. Termination via HO_2-loss is the main pathway, but this is contingent on the O_2-addition site which is prone to uncertainty. Experimental results indicate that BPR formation from this pathway takes place.

Table S10: Rate coefficients for para-cresol p4 (methyl-ipso) BPRs at T=298.15 K

Reaction	Rate (s^{-1})
O2add1*	$3.9 \cdot 10^5$
O2add2*	$2.0 \cdot 10^3$
O2add_endo	7.1
O2add1-HO2*	$2.1 \cdot 10^{10}$

*Pseudo-unimolecular rates calculated for O_2 concentration of $5 \cdot 10^{18}$ $\#/cm^3$

S11: 1,5 H-shift channel in para-cresol.

Unlike the other BPRs, the p4 BPR has a 1,5 H-shift available that has a rate of $2.8 \cdot 10^5$ s^{-1} and it thus outcompetes the molecular rearrangement. The resulting structure can then add O_2. The resulting ring-retaining O_8 compounds can potentially undergo a molecular rearrangement reaction. The calculated rate coefficients at ωb97-level of theory are quite slow, but they are similar to the initial BPR molecular rearrangement. The F12-level calculations are not available for the O_8 compound due to prohibitively expensive memory requirements. The relatively slow molecular rearrangement rates indicate that ring-retaining O_8 compounds likely accumulate on

the experimental time scale and could explain the prominent O_8 signal seen in the para-cresol spectra.

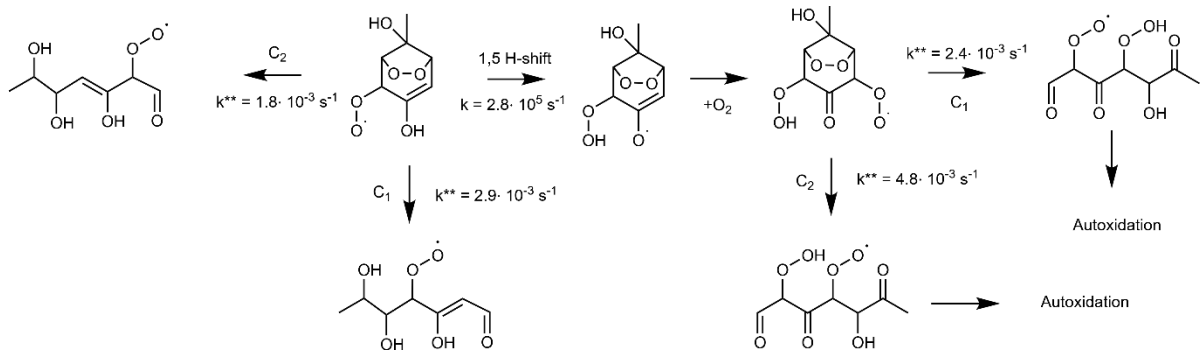

Fig. S16: 1,5 H-shift for para-cresol BPR. A fast 1,5 H-shift can result in ring-retaining O_8 compounds that can then undergo molecular rearrangement with similar rate coefficients to that of the corresponding BPR. This will result in ring-opened structures that can autoxidize further. **Rate coefficients calculated at the ωB97-level of theory.

S12: Other paths to ring-retaining O_8

As was seen for para-cresol, a 1,5 H-shift could be an atmospherically viable oxidation pathway for cresol BPRs. These pathways are considered in more detail in Figures S17 and S18 to exclude the possibility of HOM formation from these pathways. We can simplify the assessment by assuming that direct H-shifts from the methyl group are a minor pathway without excess energy as is the case for methyl-substituted, non-oxygenated aromatics [7]. No pathways to the formation of highly oxygenated molecules are known to result from methyl H-shifts of this kind for non-oxygenated compounds. Therefore, the presence of the methyl group only alters the rates of the reactions considered in Fig. S18. The geminal diol case has already been considered in the previous sections of this supplementary material. Ortho-position addition can only lead to structures with a possible 1,6 H-shift which are sterically hindered due to the large span (see OH-L in Table S8). Para-position addition can potentially lead to 1,7 H-shifts, but these likely are also slow due to the same reason. These are both seen in Fig. 17)

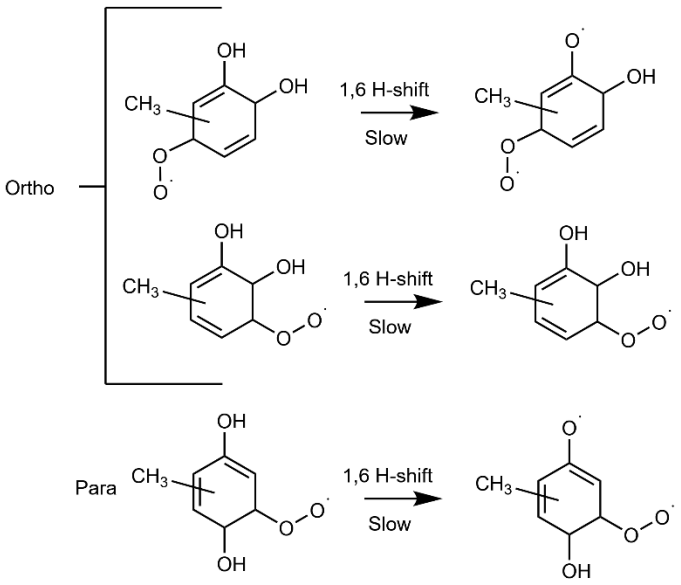

Figure S17: Cresol autoxidation. Ortho- and para-position OH-addition would require a 1,6 H-shift in order for the phenolic OH group to participate in the autoxidation.

Meta-position addition could potentially lead to 1,5 H-shifts that are atmospherically viable. Formation of ring-retaining O_8-compounds could potentially be possible if endocyclization is fast. This is likely the fate of these products, as molecular rearrangement of the resulting structures is likely slow. This is because the structures are very similar to BPRs formed from OH-addition to non-substituted carbon atoms, and their molecular rearrangement rate coefficients were systematically found to be slow (See Table S4, also [7])

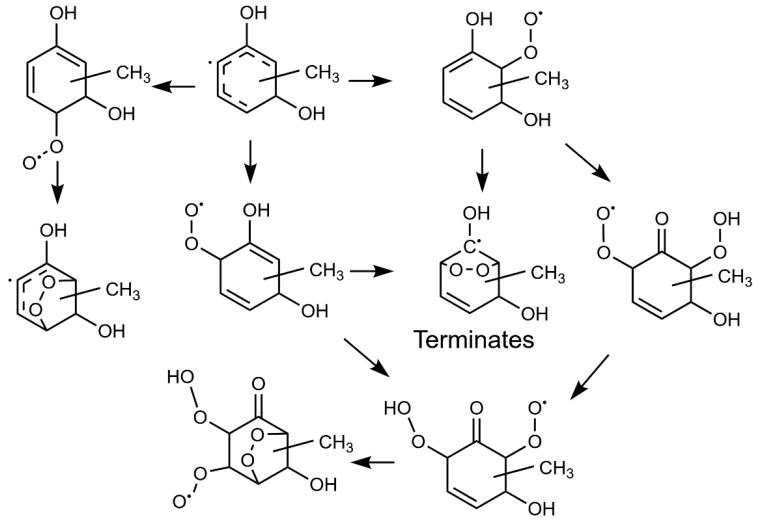

Figure S18: Formation of ring-retaining O8 species from meta-position OH-addition. The H-shift from the methyl group is ignored as it is unlikely to take part in the autoxidation based on the understanding of aromatic autoxidation. The 1,5 H-shift can potentially lead to ring-retaining compounds with 6 or even 8 oxygen atoms. These both have 2 labile H-atoms. The meta-addition channel is a minor pathway for all cresols.

S13: Meta-cresol (m1, m5)

As the m5 pathway (<0.1% OH-addition yield) is initiated by OH-addition to the meta-position, the fate of the m5 pathway is to either undergo a 1,5 H-shift at the peroxy radical stage, as was described in section S12, or to terminate via HO_2 loss following O_2-addition to the alkyl radical. This pathway is thus unlikely to explain the observed HOM.

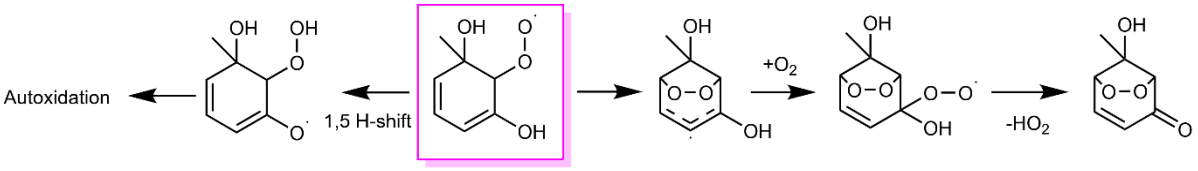

Fig. S19: Fate of the m5 pathway. The oxidation is terminated by HO_2 loss at the alkyl radical stage

The geminal diol m1 pathway (<0.1% OH-addition yield) will likely form similarly to ortho- and para-cresol. Once they form, the molecular rearrangement rate coefficients are very fast. The available H-shifts following molecular rearrangement of meta-cresol geminal diol BPRs are similar to those of the other cresols. The likely fate of m1-L (Fig. 20a) and m1-R (Fig. 20b)

is the formation of O_8-compounds via 1,6 aldehydic H-shift, but the formation of O_{10}-compounds is also possible via the C2 pathway. The geminal diol pathway is thus likely the source of the observed HOMs.

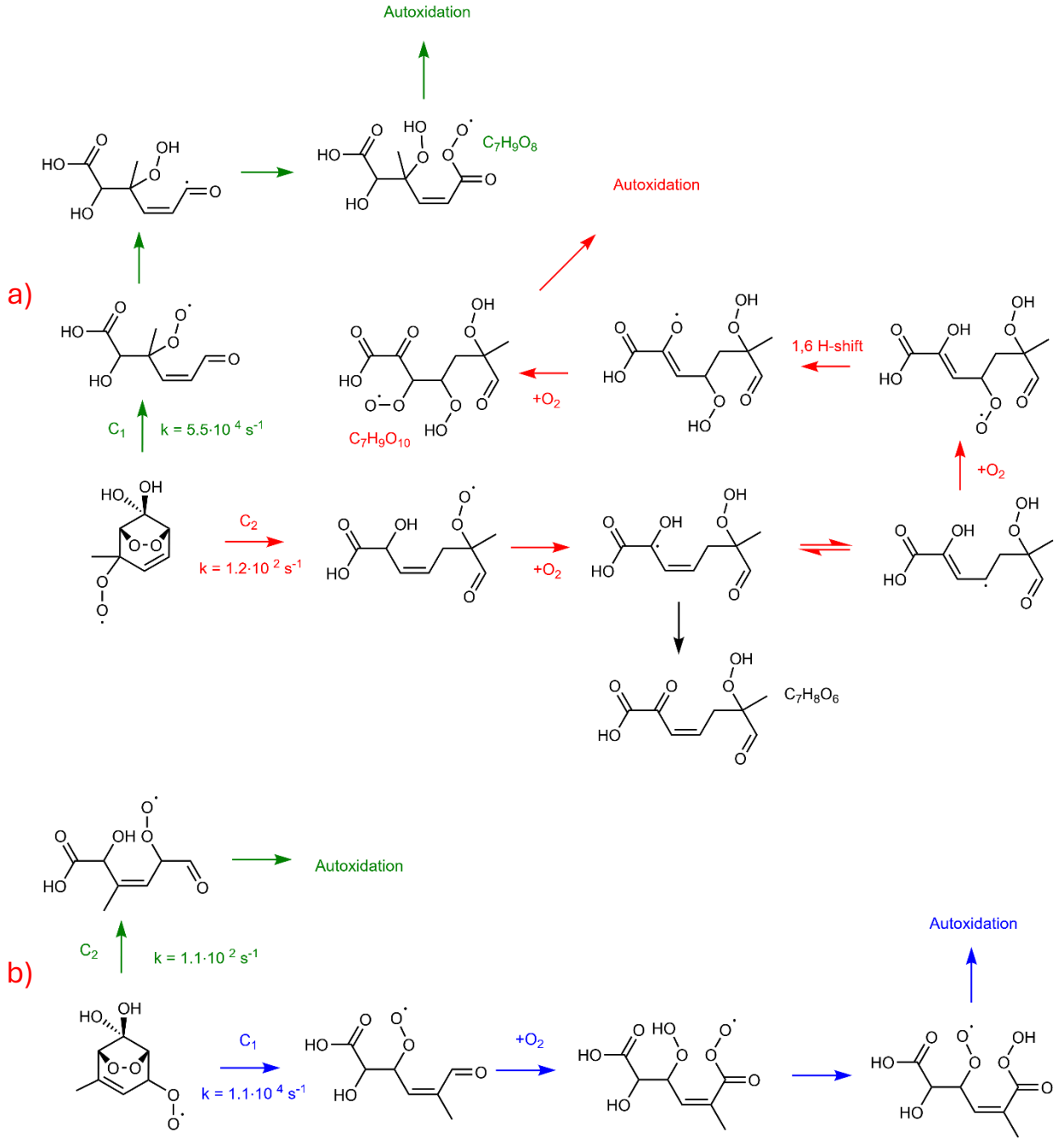

Fig. 20: Meta-cresol autoxidation. Due to the similarity between the available H-shift between the cresols, the following pathways have been inferred based on oxidation mechanism of ortho- and para-cresol. The main fate of both of the pathways is the formation of O_8-compounds via an aldehydic 1,6 H-shift which could oxidize further.

S14: Other phenolic compounds

To demonstrate the generality of the geminal diol pathway, the geminal diol OH-addition branching ratios and the subsequent molecular rearrangement rate coefficients were

determined. Phenol, 2-ethylphenol, 2,5-dimethylphenol, guaiacol and 2-naphtol were chosen as a varied and a representative sample. Phenolic compounds can form as a result of OH initiated oxidation, and OH-addition to ortho-position is most favoured. For this reason, 2-ethylphenol, 2,5-dimethylphenol, guaiacol are the highest yield phenolic products from OH-initiated oxidation of ethylbenzene, para-xylene and anisole respectively. 2-naphtol was chosen over 1-naphtol, as forming a geminal diol BPR from 1-naphtol would require the endoperoxide bridge to connect to the tertiary carbon. It is not known how the second aromatic ring affects the BPR formation in naphtol oxidation, and thus 2-naphtol was chosen to bypass this complication. The OH-addition branching ratios have previously been determined for phenol [22] and guaiacol [23], yielding values 1.4% and 12.4% respectively. For the other compounds, the OH-addition rate coefficients are calculated in Table S11, from which branching ratios are calculated in Table S12 using equation 2, with the used notations presented in Fig. S21.

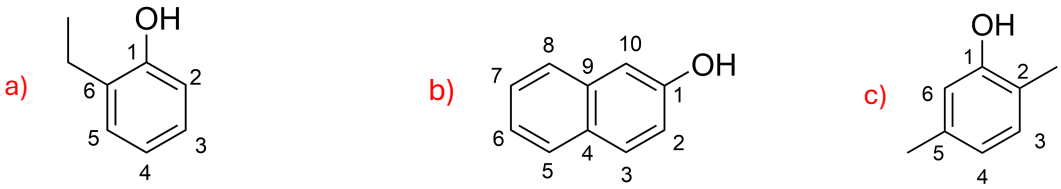

Fig. S21: Notations used for OH-addition sites to phenolic compounds. a) 2-ethylphenol b) 2,5-dimethylphenol c) 2-naphtol.

Table S11: Bimolecular rate coefficients for OH-addition and H-abstraction, F12 level, T=298.15 K ($cm^3\ molecule^{-1}\ s^{-1}$)

	1	2	3	4	5	6	7	8	9	10
2-ethylphenol	$3.15 \cdot 10^{-14}$	$7.25 \cdot 10^{-13}$	$2.03 \cdot 10^{-15}$	$1.01 \cdot 10^{-14}$	$1.12 \cdot 10^{-14}$	$9.33 \cdot 10^{-14}$	-	-	-	-
2-naphtol	$3.76 \cdot 10^{-14}$	$9.55 \cdot 10^{-13}$	$5.62 \cdot 10^{-14}$	$7.57 \cdot 10^{-19}$	$1.57 \cdot 10^{-13}$	$3.47 \cdot 10^{-14}$	$7.71 \cdot 10^{-15}$	$1.32\text{-}4.36 \cdot 10^{-13}$**	$7.25 \cdot 10^{-20}$	$2.01 \cdot 10^{-11}$
2,5-xylenol	$2.64 \cdot 10^{-13}$	$2.99 \cdot 10^{-12}$*	$2.55 \cdot 10^{-14}$	$1.56 \cdot 10^{-13}$	$6.89 \cdot 10^{-14}$	$5.30 \cdot 10^{-13}$	-	-	-	-

*=m062x

**CCSD-calculation fails to converge for the lowest energy conformer. The higher energy conformer yields a rate of $1.32 \cdot 10^{-13}\ cm^3\ molecule^{-1}\ s^{-1}$ and the gibbs energy difference for the two conformers at the ωb97-level of theory is 0.7 kcal mol. Subtracting this energy difference from the barrier F12-barrier for the high energy conformer yields a rate of $4.36 \cdot 10^{-13} \cdot 10^{-13}\ cm^3\ molecule^{-1}\ s^{-1}$.

Table S12: Branching ratios, F12 level, T=298.15 K ($cm^3\ molecule^{-1}\ s^{-1}$). The geminal diol positions are bolded.

	1	2	3	4	5	6	7	8	9	10
2-ethylphenol	**3.61**	83.0	0.23	1.16	1.29	10.7	-	-	-	-
2-naphtol	**0.17**	4.39	0.26	0.00	0.72	0.16	0.04	2.01**	0.0	92.25
2,5-xylenol	**6.55**	74.10 *	0.63	3.87	1.71	13.14	-	-	-	-

=m062x

**using the higher rate of $4.36 \cdot 10^{-13}\ cm^3\ molecule^{-1}\ s^{-1}$.

The molecular rearrangement rate coefficient are presented in Table S13 and the corresponding transition states are presented in Figure S22. All of the rates are in excess of 100 s^{-1}.

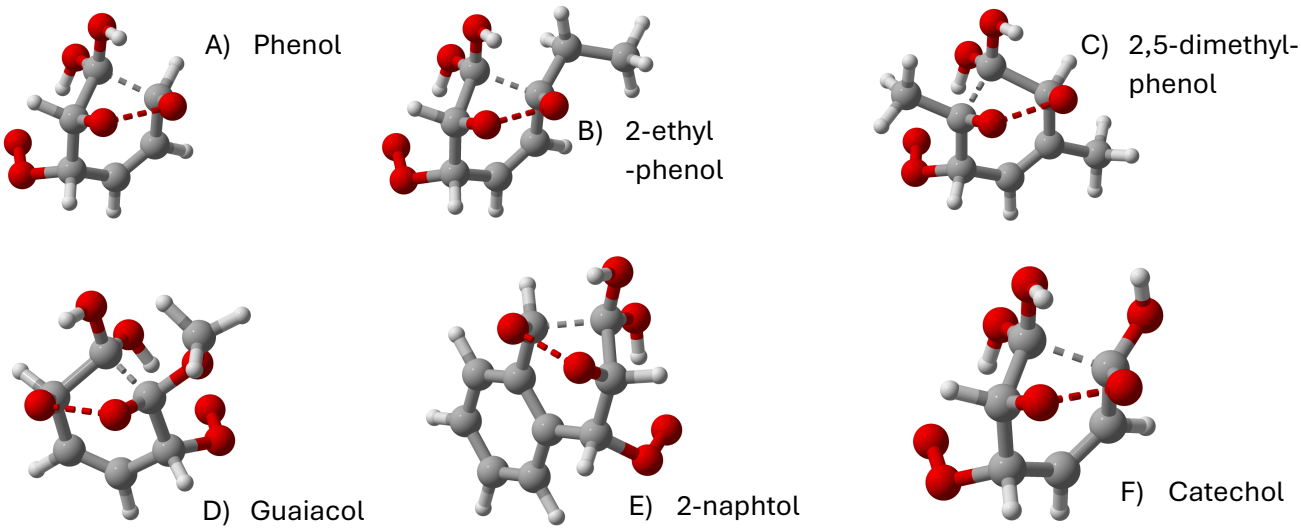

Fig. S22: Molecular rearrangement transition states for the geminal diol BPR formed from different phenolic compounds. The compounds are A) phenol, B) 2-ethylphenol, C) 2,5-dimethylphenol, D) guaiacol, E) 2-naphtol and F) Catechol.

Table S13: Rate coefficients (s^{-1}) for molecular rearrangement of phenolic compounds. Lowest conformer transition state theory used with F12-level of theory at T=298.15K. Tunneling corrections were not calculated.

	Phenol	2-ethylphenol	2,5-dimethylphenol	Guaiacol	2-naphtol	Catechol
Rate	$1.02 \cdot 10^4$	$8.71 \cdot 10^2$	$3.83 \cdot 10^3$	$1.79 \cdot 10^2$	$1.18 \cdot 10^3$	$9.53 \cdot 10^2$

Following molecular rearrangement, the ring-opened peroxy radicals of these phenolic compounds have similar autoxidation pathways as the cresol isomers and likely lead just as efficiently to highly oxygenated peroxy radical molecules. This is corroborated by OH oxidation experiments of 2-naphtol we carried out (see section S22).

S15: Geminal diol pathway in 3-methylcatechol

The rate coefficients for OH-addition to 3-methylcatechol were calculated to determine the geminal diol OH-addition yield. The rates are shown in Table S5.2b with the notation used shown in Fig. S23.

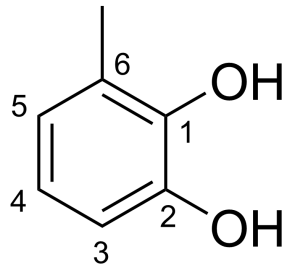

Fig. S23: OH interaction sites for 3-methylcatechol.

Table S14: Bimolecular rate coefficients for OH-addition ($cm^3\ molecule^{-1}\ s^{-1}$) at T=298.15 K

	1	2	3	4	5	6
Rate	$4.43 \cdot 10^{-11}$	$7.15 \cdot 10^{-12}$	$5.41 \cdot 10^{-13}$	$2.24 \cdot 10^{-14}$	$4.19 \cdot 10^{-14}$	$8.38 \cdot 10^{-14}$
Branching ratio	85.0	13.7	1.0	0.0	0.1	0.2

As for cresols, the OH-abstraction channels at the F12-level of theory values suffer from the aforementioned issues [2]. For this reason, the ωb97-level of theory values are also presented. These are $8.35 \cdot 10^{-10}$, $9.45 \cdot 10^{-11}$, $1.01 \cdot 10^{-10}$, $3.05 \cdot 10^{-12}$, $5.01 \cdot 10^{-12}$, $6.21 \cdot 10^{-12}$, $8.32 \cdot 10^{-11}$, $1.15 \cdot 10^{-10}$, $2.59 \cdot 10^{-10}$ $cm^3\, molecule^{-1}\, s^{-1}$ for addition to positions 1,2,3,4,5,6 methyl abstraction, OH(1)-abstraction, OH(2)-abstraction. The values indicate that abstraction accounts for roughly 30 % of the reactions with OH. As was discussed in section S1 this is likely overestimated as H-abstraction from phenolics is a minor pathway.

Further oxidation requires O_2-addition to the two ortho-positions in relation to the OH-addition site, with para-position addition likely being reversible. The structure is symmetric relative to the aromatic ring, and thus there are only possibilities presented in Fig. S24. Of the two ortho-position addition sites, addition to the OH-substituted carbon leads to termination via HO_2-loss, whereas the other leads to endocyclization. Computing accurate branching ratios using DFT methods is not possible, but rates for O_2-addition are presented in table S15. These rate coefficients would indicate a close to 100 % branching ratio for C(OH). For the C(OH) multiple transition states were found with Gibbs energy barriers ranging from 10.7 to 5.2 kcal/mol, but for C(CH_3) only one transition state with barrier 11.7 kcal/mol was found. Similar situation was found for p1 and o6, in which addition to C(OH) addition was favored, but the corresponding BPR compounds were still likely detected experimentally. O_2-addition reactions are likely not well described by single reference methods. In addition, the conformer sampling process might also miss some low energy conformers. This would affect the branching ratios.

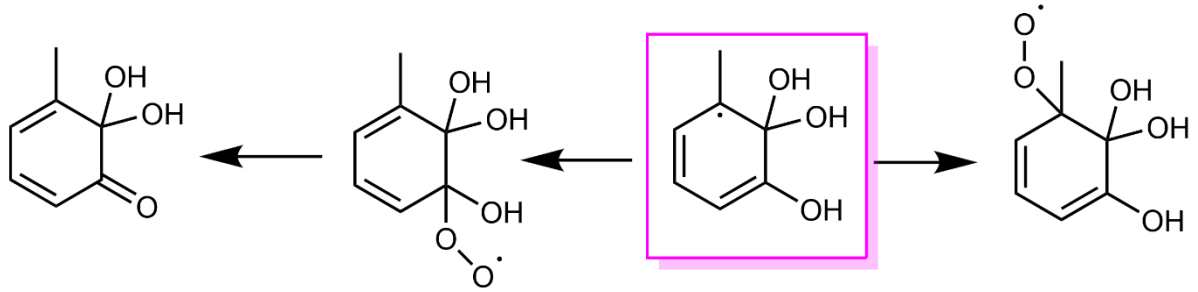

Fig. S24: O_2-addition to 3-methylcatechol.

Table S15: O_2-addition rate coefficients to 3-methylcatechol.

	C(OH)	C(CH_3)
Rate coefficient (s^{-1})*	$5.6 \cdot 10^5\ s^{-1}$	$3.1 \cdot 10^3\ s^{-1}$

*Pseudounimolecular rate with $[O_2] = 5 \cdot 10^{18}\ \#/cm^3$

Following O_2-addition, endocyclization can take place. The corresponding rates are presented in Table S16 with the reaction illustrated in Fig. S25.

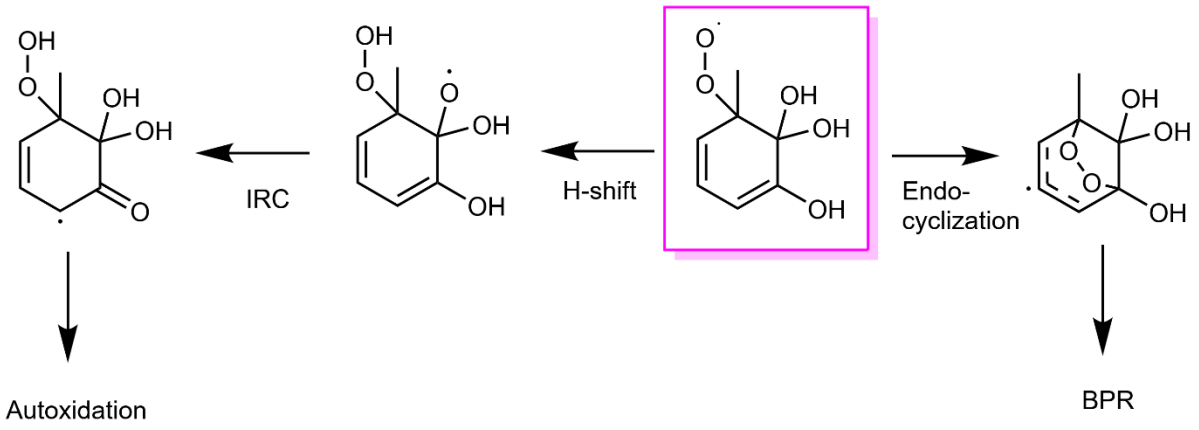

Fig. S25: Endocyclization of 3-methylcatechol.

Table S16: Endocyclization of 3-methylcatechol.

	Rate coefficient (s^{-1})	Branching ratio
H-shift (ωb97)	1100	13.9
Endocyclization	$4.8 \cdot 10^3$	86.1

The barriers are 11.3 kcal/mol and 15.0 kcal/mol for endocyclization and the OH H-shift respectively, with the H-shift having an imaginary frequency of -1570 cm^{-1}. The H-shift pathway is a multi-step reaction, with another H-shift happening in the IRC, leading to the formation of a geminal diol. Using the endpoints of the IRC will again lead to an overestimation of the tunneling factor. In analogy with the cresol (See section S3.1) tunneling factor of 50 was used.

Endocyclization is followed by O_2-addition to form a BPR. The molecular rearrangement rates at LC-TST are presented in Table S17 and the molecular rearrangement opening direction is shown in Fig. S27. Breaking these bonds is the only energetically favored way, since breaking the other C-C bond would lead to a geminal diol intermediate, similar to BPRs formed from ortho-position OH-addition for the cresol isomers.

Table S17: Molecular rearrangement rate coefficients (s^{-1}) using lowest-conformer transition state theory for two 3-methylcatecol geminal diol isomers.

	C2	C1
Rate coefficient	7.4	2.7

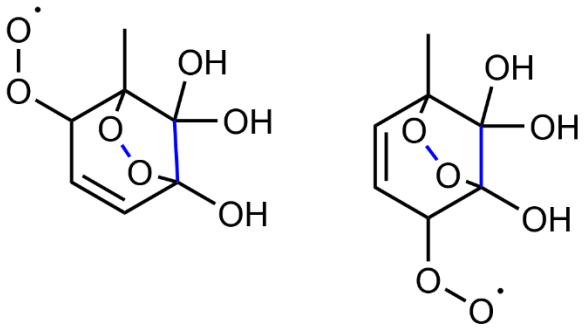

A) C2

B) C1

Fig. S26: Notations used for two geminal diol BPRs from 3-methylcatechol

The relatively slow molecular rearrangement rate coefficients relative to the molecular rearrangement rates are likely due to the stability of the lowest energy reactant conformer. This is seen in Fig. S28.

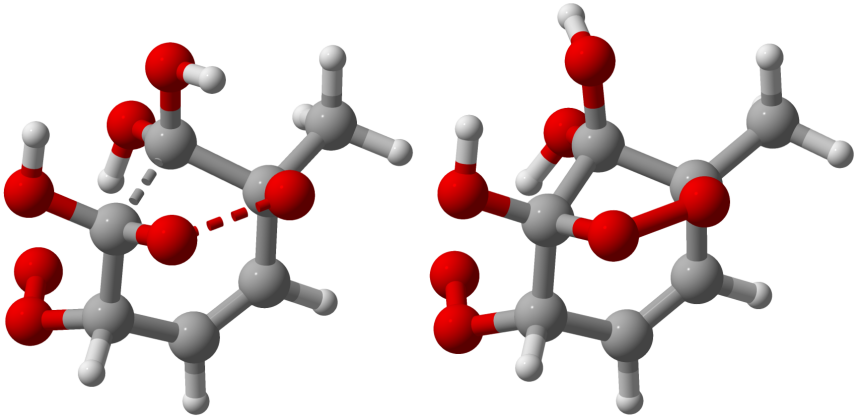

Fig. S27: Notations used for two geminal diol BPRs from 3-methylcatechol

There is no fast reaction pathway following molecular rearrangement (1,6 H-shift, aldehydic H-shift) and thus the fate of the compounds is likely to thermalize.

Simulations

Chemical mechanisms

S16: Geminal diol pathway

The geminal diol pathway developed in this paper leads to the formation of highly oxidized compounds. Due to the high abundance of oxygen-containing functional groups, they are likely very effective at forming molecular clusters and contributing to SOA growth. To quantify this, the geminal diol mechanism was incorporated into a toluene SOA model to quantify its effect on multi-generational toluene SOA formation and compared to results without this pathway. The oxidation mechanism of both ortho-cresol, and its oxidation product 3-methylcatechol are incorporated.

Ortho-cresol geminal diol pathway

To simplify the model, only the main (blue) pathway in Fig. 4 of the manuscript was implemented, with a branching ratio of 87.3%. A branching ratio of 6% was used for OH-addition to the geminal diol position, of which 70% goes to geminal diol BPR formation and 30% goes to a closed shell carboxylic acid species $C_7H_8O_3$ (condensable). Further oxidation of the geminal diol BPRs by NO and HO_2 is considered. Fast unimolecular rearrangement leads to ring-opened RO_2 compounds, that can undergo autoxidation. The first 1,6 H-shift and the following O_2-addition can form a second closed-shell carboxylic acid $C_7H_8O_6$ and an RO_2 compound $C_7H_9O_8$ with assumed branching ratios of 50% for each. This peroxy radical undergoes a second autoxidation step to form the carboxylic acid $C_7H_9O_{10}$. Subsequent oxidation reactions are not considered, as the species is almost exclusively present in the particulate phase due its low saturation vapor pressure.

Modification of the 3-methylcatechol pathway

For 3-methylcatechol, a branching ratio of 80% was used for OH-addition to the geminal diol position based on our computations (see Table S14) Following OH-addition, there are two possible O_2-addition as illustrated in Fig. S24. Equal branching ratios were assumed, meaning 50% are expected to form the ring-retaining closed-shell $C_7H_8O_3$ (see Fig. S24) and the other 50% forming the geminal diol BPR. To simplify the model, the endocyclization branching ratio was assumed to be 100%. A rate coefficient of 7.4 s^{-1} is used for the molecular rearrangement of the BPR, based on our calculations (Table S17). This results in the formation of a ring-opened dicarboxylic acid $C_7H_9O_7$ RO_2 that likely has slow subsequent autoxidation pathways due to the lack of labile H-atoms. Consequently, further oxidation products were not considered.

Toluene SOA chemical schemes including other pathways

The new geminal diol pathways were added to the quasi-explicit toluene SOA scheme of [31] that was already supplemented with the molecular rearrangement of the ipso bicyclic peroxy radical (BPR) of toluene [7, 38]. The quasi-explicit mechanism of [31] was adapted from the Master Chemical Mechanism v3.3.1 [26, 29] to which several oxidation pathways were added: multihydroxylation [21], the formation of heterocyclic compounds [28], the irreversible partitioning of methylglyoxal, the Highly Oxygenated organic Molecules (HOM) formation without ring opening [40]. This scheme leads to the formation of 104 semi-volatile species representing toluene SOA.

To reduce computational complexity, the quasi-explicit chemical mechanism of toluene SOA was reduced using the GENOA algorithm [41], keeping only the main SOA formation pathways [38]. The ipso BPR pathway of [7] was integrated in this reduced mechanism, leading to the "rdc M3" mechanism described in [38], hereafter referred to as the M3 mechanism, with only 14 semi-volatile species representing toluene SOA formation.

Inclusion of the geminal diol pathway in the other chemical schemes

The geminal diol pathway developed in this paper is added to both the quasiexplicit and the reduced toluene SOA scheme. To do so, in the OH oxidation reaction of cresol and methylcatechol, the branching ratios are adapted to assess the formation of geminal diol BPR, respectively 6% and 80%. The following main reactions, rearrangement, H-shift and O_2-addition are integrated using the rate coefficients and branching ratios calculated previously. The saturation vapor pressure and the enthalpy of vaporization of the semi-volatile compounds added to the chemical schemes are computed using the software UManSysProp [39] with [32] coupled [33] for the boiling points, as described in Table S18.

Table S18: Saturation vapor pressure (Psat, in torr) and enthalpy of vaporization (dHvap, in kJ/mol) of the semi-volatile species from the geminal diol mechanism.

Species	Psat	dH_{vap}
C7H8O3 CRES	xxx	xxx
C7H8O3 MCAT	$2.55 \cdot 10^{-3}$	79.5
C7H8O6	$5.67 \cdot 10^{-8}$	127.0
C7H9O10	$4.85 \cdot 10^{-17}$	227.0
C7H9O7	$1.12 \cdot 10^{-12}$	180.0

Flow tube experiments with quasi-explicit chemical mechanisms

The impact of the newly implemented pathways on toluene SOA concentrations simulated in a flow-tube experiments is studied. The experimental setup is described in [31]. Toluene SOA is formed in an aerosol flow tube exposed to UV-lamp irradiation, into which ammonium sulfate seed particles, toluene, and isopropylnitrite (IPN) are introduced at high concentrations. The oxidation of toluene is modeled using the quasi-explicit toluene chemical mechanism from [31], with the added pathway accounting for a molecular rearrangement involving ring opening of a bicyclic peroxy radical (BPR) [7].

Toluene's aging was simulated using this mechanism in the box-model SSH-aerosol v2.0 [35, 37]. Photolysis kinetic rates are adapted to the experimental UV light emissions, physical parameters (RH,T) and initial concentrations of seed and precursor are constrained by the experimental setup. The simulation also incorporates wall losses of stable gaseous and particle compounds and the irreversible condensation of glyoxal and methylglyoxal. Details regarding radical equilibrium, IPN chemistry, and experimental conditions are provided in [30]. The interactions in the particle phase are assumed to be ideal here [37].

Simulations including or not the geminal diol mechanism on toluene SOA formation are compared in Fig. S28. Including the geminal diol mechanism has a low impact on SOA mass: the total SOA mass is almost unchanged using the quasi-explicit scheme with and without the geminal diol mechanism. However, the chemical composition of the SOA is notably different. Dicarboxylic compounds ($C_7H_9O_9$), which were not accounted for in the previous mechanism, now contribute significantly: up to 45% of the total SOA mass. Other condensable species introduced via the geminal diol pathway are less dominant but still contribute non-negligibly, especially the carboxylic acids $C_7H_9O_{10}$ and $C_7H_8O_6$ (respectively 6% and 5% of the total SOA mass).

S17 0D atmospheric simulations with quasi-explicit chemical mechanisms

Box simulations of atmospheric conditions are performed with SSH-aerosol v2.0. As detailed in [37], initial gas concentrations are taken to be representative of the atmospheric conditions simulated by [36] over Greater Paris in July 2009. The initial NO_2 concentration is taken equal to 26 μg m^{-3}, and the simulated OH concentration varies between 1.2 and 7.6 x 10^{-4} μg m^{-3}. Low values are used for initial organic and inorganic aerosol concentrations, to serve as a condensation core. To keep the particle dynamic as simple as possible, only one size section (representing aerosol with diameters between 0.1585 μm and 0.4 μm) is used. The simulations are run for about 5 hours with outputs every minute using both the quasi-explicit toluene SOA scheme and the extended version incorporating the geminal diol mechanism.

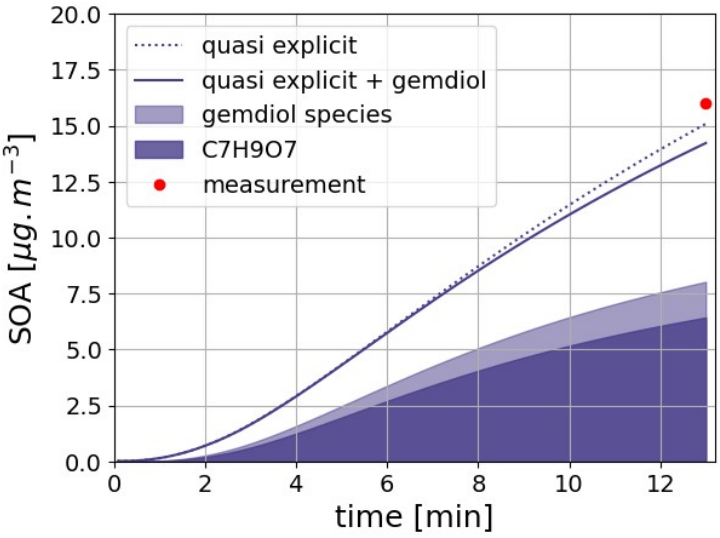

Fig. S28: Time evolution of toluene SOA mass using different chemical mechanisms for the flow tube experiment of [31, 37].

Figure S28 shows the time-variation of the toluene and cresol SOA in the simulations. After 5 hours of simulation, the toluene SOA mass is about 23% higher when the geminal diol mechanism is incorporated. The $C_7H_9O_7$ compound from the geminal diol mechanism represents about 19% of the toluene SOA mass. This compound represents as much as 69% of the cresol SOA mass. Most of it is formed by the geminal diol pathway, which represents about 88% of the cresol SOA mass. This results in a substantial increase in the cresol contribution to toluene SOA mass, up to three times higher than in simulations using the quasi-explicit scheme without the geminal diol mechanism.

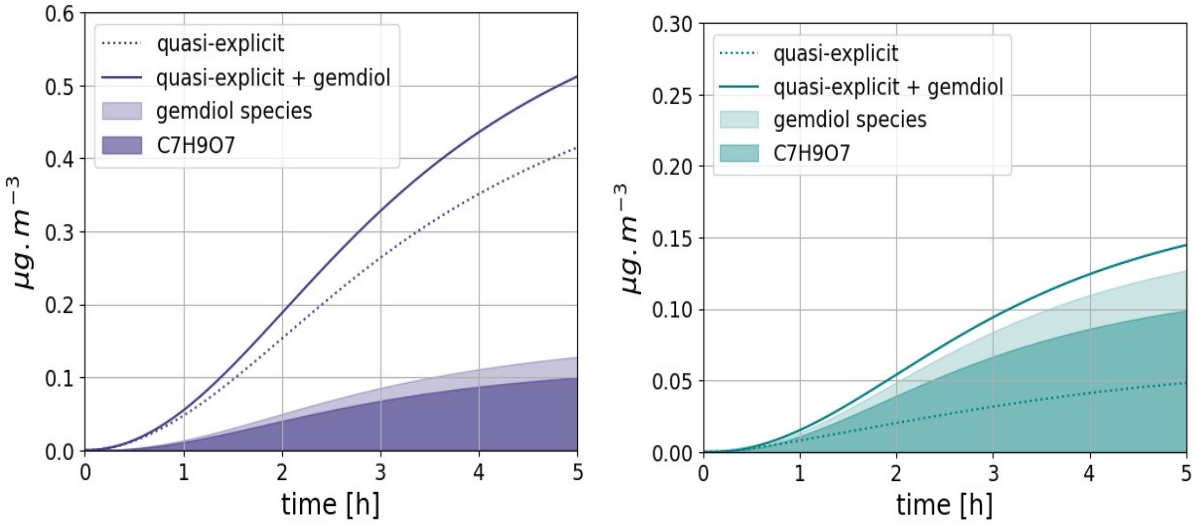

Fig. 29: Time evolution of toluene and cresol SOA mass using several chemical mechanisms and the atmospheric conditions described in [13].

S18: 3D simulations with reduced chemical mechanisms

Simulations are conducted over one month over Greater Paris with a horizontal resolution of 0.02° x 0.02°, starting on 6 May 2014, using the modeling chain WRF-Polair3D/SSH-aerosol. Meteorological conditions are modeled using the WRF model (version 3.9.1.1). Gaseous chemistry and aerosol dynamics are taken into account. The size distribution of particles is represented by 6 size sections of diameters ranging between 0.01 and 10 μm: [0.01 – 0.0398 μm], [0.0398 – 0.1585 μm], [0.1585 – 0.4 μm], [0.4 – 1 μm], [1 – 2.5119 μm] and [2.5119 – 10 μm]. Gaseous chemistry involves 161 gas-phase species and 47 particle-phase species, amongst which 13 are semi-volatile from the M3 mechanism. Anthropogenic emissions are retrieved from the EMEP/European Environmental Agency gridded emission inventory, and biogenic emissions from the MEGAN model [27]. The set-up is the same as in [34, 38]. The model validation by comparisons to measurements of BC, NO_2, PM_{10}, $PM_{2.5}$, and organic matter is presented in [34, 38]. Here, a sensitivity simulation is performed using the M3 mechanism supplemented with the geminal diol mechanism for toluene SOA formation, leading to 17 semi-volatile species from toluene SOA. The impact of the toluene SOA scheme on the simulated toluene SOA mass is low (less than 4%). Fig. S30 shows the concentrations of toluene SOA, and the differences between simulations that use the M3 mechanism and the M3 supplemented by the geminal diol mechanism. However, the impact on the toluene SOA composition is high. As shown in Fig. 5a of the main manuscript, using the M3 mechanism, most of the toluene SOA is formed from the ipso-BPR pathway (C7H9O9, 60.8%). The cresol pathway represents about 16.4% of toluene SOA (6.9% from methylnitrocatechol MNCATECH, 4.4% from multihydroxylation, 5.1% from HOM2ONO2, which is formed partly from the oxidation of methylnitrocathecol). The cresol pathway is more important with the implementation of the geminal diol mechanism and represents 33.2% of the toluene SOA: 12.0% from the previously implemented pathways (5.5% from methylnitrocatechol MNCATECH, 4.0% from multihydroxylation, 2.5% from HOM2ONO2), and 21.2% from the geminal diol mechanism (17.0% from C7H9O7, 2.4% from C7H9O10 and 1.8% from C7H8O6). The predominance of the newly implemented pathways in the cresol SOA composition is illustrated in Fig. 5b: it contributes to about 61.2% of the cresol SOA mass. The C7H9O7 compound from methylcatechol oxidation represents most of it: 49.1% of the cresol SOA mass, while the C7H9O10 compound represents 7.0% and C7H8O6 about 5.1%. Additionally, as can be seen in the Fig. S31, inclusion of the geminal diol pathways increased the cresol SOA mass concentrations by 9-12%.

The 3D simulation presented here does not include primary emissions of cresol. However, the chemical pathways implemented would be especially relevant when investigating sources with high cresol emissions, such as agricultural activities and biomass burning.

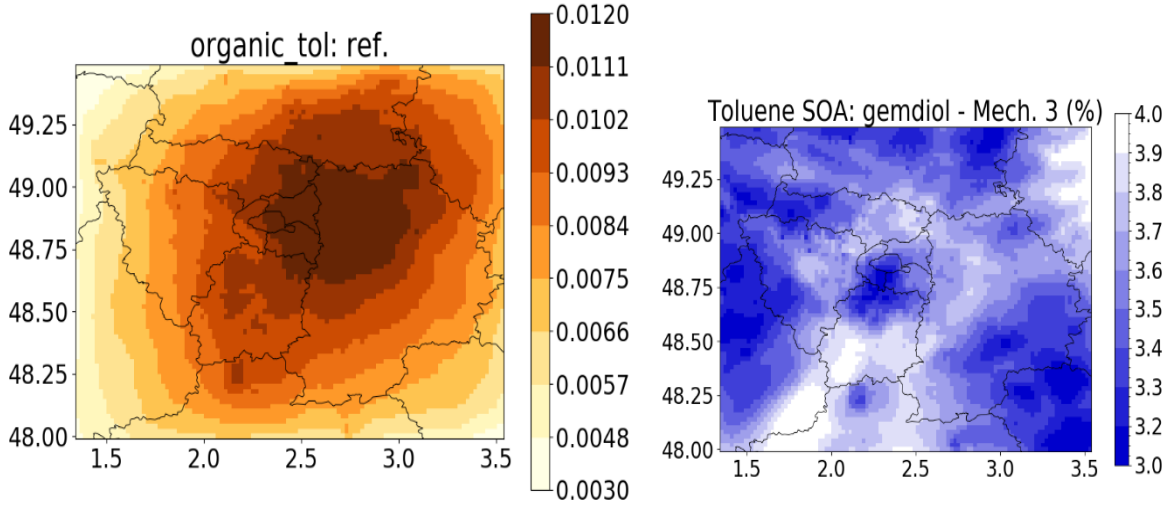

Fig. 30: Toluene SOA mass concentrations between 6 May - 6 June 2014 with the M3 chemical scheme (left panel) and relative differences (%) of toluene SOA concentrations simulated using the M3 + gemdiol chemical scheme and the M3 scheme (right panel).

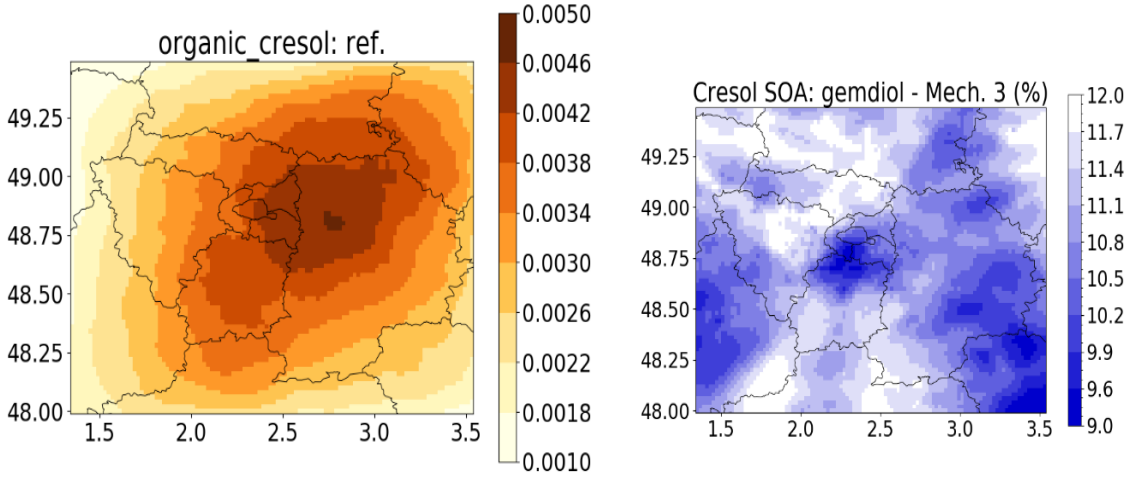

Fig. S31: Cresol SOA mass concentrations between 6 May - 6 June 2014 with the M3 chemical scheme (left panel) and relative differences (%) of cresol SOA concentrations simulated using the M3 + gemdiol chemical scheme and the M3 scheme (right panel).

Experimental

S19: H_2O_2-photolysis experiments

Experiment set up.

Flow tube reactor experiments coupled with NO_3^--based chemical ionization mass spectrometry (CIMS) were performed to study the gas-phase oxidation products of the cresol isomers. H_2O_2 photolysis was used as a source of OH radicals, with the radicals being photolyzed using a germicidal lamp (λ_max = 254 nm). The spectra are presented in Fig. S32 and the peak list is presented in Table S19. The residence time was varied from 0.9 to 1.9 seconds using a movable injector placed inside the flow reactor and the experiments were conducted at room temperature and atmospheric pressure, with zero air used as the bath gas. All gas flows were regulated by calibrated mass flow controllers (Alicat Scientific), which were used to calculate the concentration of the reactants in the gas mixture.

A CI-APi-TOF was used to measure the product signals (Tofwerk Aerodyne Research Inc.) using an Eisele-type CI inlet (Eisele) [24]. UHP nitrogen flowing through the conc. HNO_3 was introduced into the inlet which was further exposed to soft X-rays (< 9.5keV, Hamamatsu L9490) to produce NO_3^-. The sheath air flow inside the inlet which contains unionized HNO_3 and NO_3^-, mixes with the sample gas flow and thus induces the ionization. Specifically, NO_3^- formed an adduct (HNO_3*NO_3^-) with neutral HNO_3, which could be displaced by analyte molecules (X) only if the resulting X*NO_3^{-1} adduct had a higher binding enthalpy than that of HNO_3*NO_3^-. [25] The quartz flow tube (50 cm length and 1 inch OD) was connected to the CI-APi-TOF via the Eisele inlet. The same experimental condition of pressure (1 atm) and temperature (T = 295 ± 2 K) was maintained throughout the experiments.

The concentration of all the reactants were calculated using the flow rates and the vapor pressure and are given in Table S19. The concentration of OH radicals was determined indirectly by measuring the concentration of sulfuric acid, which is formed through the reaction of OH with SO_2. PTFE tubing (6 mm o.d.) was used for the flow of all the reagents and gases to the flow reactor via a series of cross Swagelok fittings connected upstream to the reactant flow.

Table S19. Concentration of the reactants used in the experiments.

Reagent	Concentration (molecule cm^{-3})
Initial OH	$(3.98 – 5.57) \times 10^6$
NO	$(0.492 – 4.92) \times 10^{12}$
Para-cresol	$(2.03 – 6.08) \times 10^{11}$
Meta-cresol	$(1.93 – 5.79) \times 10^{11}$
Ortho-cresol	$(0.22 - 1.10) \times 10^{12}$

All data processing, including averaging, mass axis calibration, and peak integration, was done using the tofTools software package for MATLAB.

Chemicals

A clean and dry zero air was obtained from the zero air generator (AADCO Instruments, 737 Series) which was fed with clean in-house synthetic air. The generated zero air was further passed through a mist separator (SMC AMG 150C-F01C) and air membrane dryer (SMC IDG100LA-F04B-P) for further dehumidification, connected upstream to airflow before the experimental setup. Para cresol (liquid, purity 99.0%), meta cresol (liquid, purity 99%), ortho cresol (liquid, purity ≥99.0%), D_2O (liquid, purity 99.9 atom % D), H_2O_2 solution (50% weight in H_2O) and concentrated HNO_3 (70%) were commercially obtained from Sigma Aldrich. All the flows were measured by calibrated mass flow controllers (Alicat Scientific). All the chemicals were used without further purification.

Fig. S20: Peak list in the NO_3^- experiments

Peak	Mass
C7H9O6NO3-	251.0283
C7H9O8NO3-	283.0181
C7H9O10NO3-	315.0079
C7H9O12NO3-	346.9978

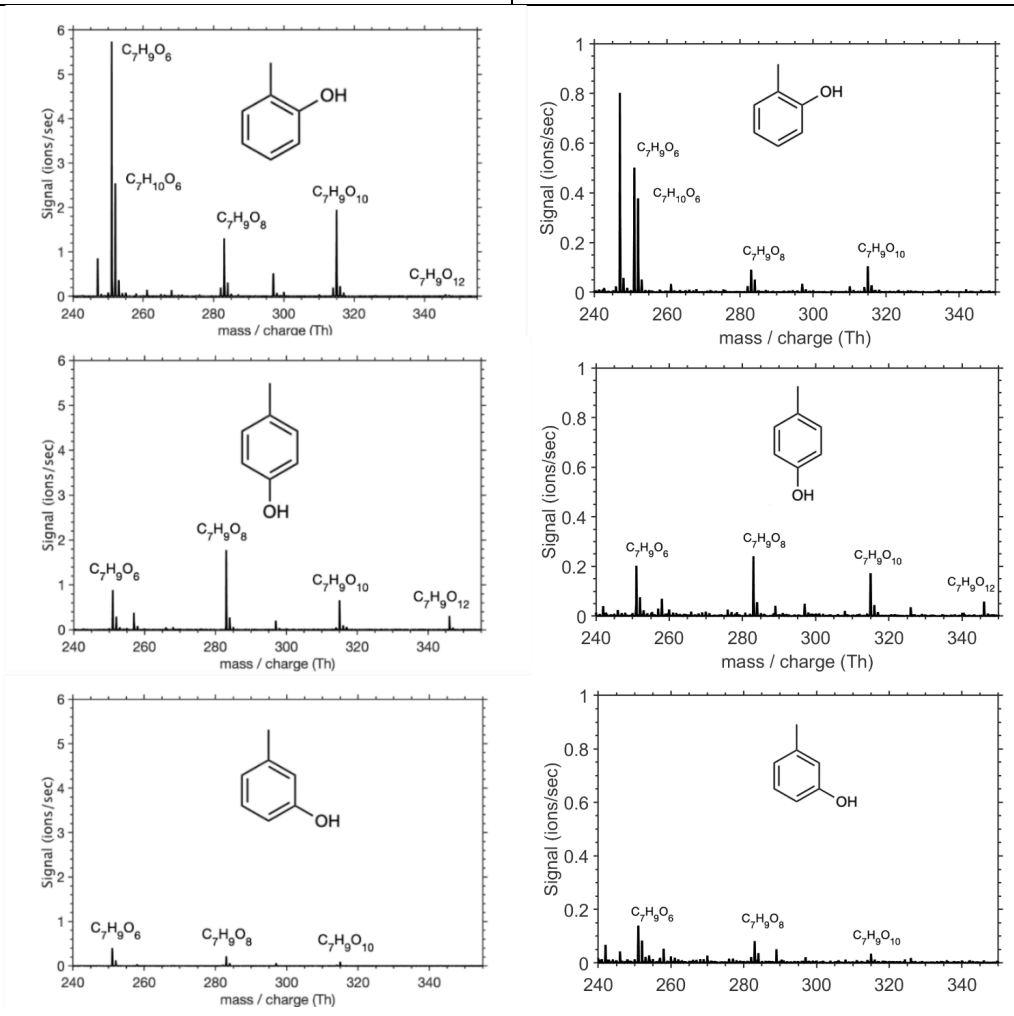

Fig. S32: Cresol spectra with two different residence times. Left: 1.9s residence time. Right: 0.9s residence time. Distribution of the shorter residence time is similar to the longer residence time and shows a similar qualitative pattern. The fact that highly oxygenated compounds are seen in sub-second timescales requires rapid unimolecular formation pathways. Peaks with an

even number of oxygen atoms from O_6 to O_{10} are seen for all cresol isomers, and O_{12} peaks are clearly seen for ortho- and para-cresol. The actual O_{12} peak is next to a relatively large background peak. The O_{12} peak likely also forms for meta-cresol, but the peak is too small to be unambiguously separated from the background noise. The O_{10} peak intensities follow the trend ortho > para > meta expected from the geminal diol pathway. The O_6 peaks also follow the trend ortho > para > meta consistent with the OH-addition yields to the methyl substituted carbon.

S20: D_2O and NO experiments

Deuterated water (D_2O) was added to gain structural information about the structures. Functional groups with labile H-atoms will interchange hydrogens with deuterium and increase the mass by a single mass unit in the process. This is experimentally detectable and reveals information about the number of labile H-atoms. The peak list for NO experiments is presented in Table S21 with the NO spectra shown in Fig. S33.

NO was added to verify that the observed molecules were indeed peroxy radicals. NO reacts with the peroxy radicals leading to the formation of organonitrates. The formation of organonitrates were observed with a simultaneous drop in the O6-O10 signal intensities when NO was added.

Table S21: Peak list in the NO experiments with NO3-CIMS

Peak	Mass	Peak (organonitrate)	Mass
$C_7H_9O_6NO_3^-$	251.0283	$C_7H_9O_5NONO_3^-$	281.0263
$C_7H_9O_8NO_3^-$	283.0181	$C_7H_9O_7NONO_3^-$	313.0161
$C_7H_9O_{10}NO_3^-$	315.0079	$C_7H_9O_9NONO_3^-$	345.0059
$C_7H_9O_{12}NO_3^-$	346.9978	$C_7H_9O_{11}NONO_3^-$	376.9957

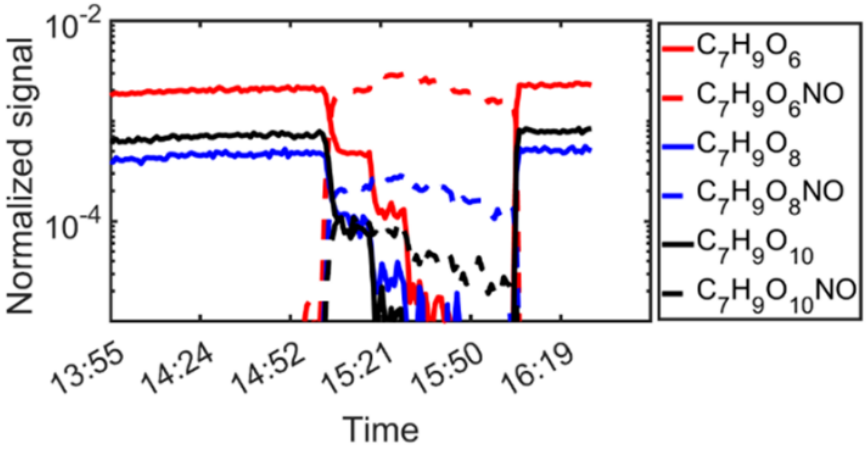

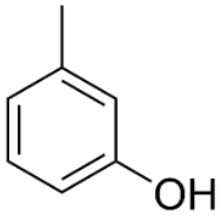

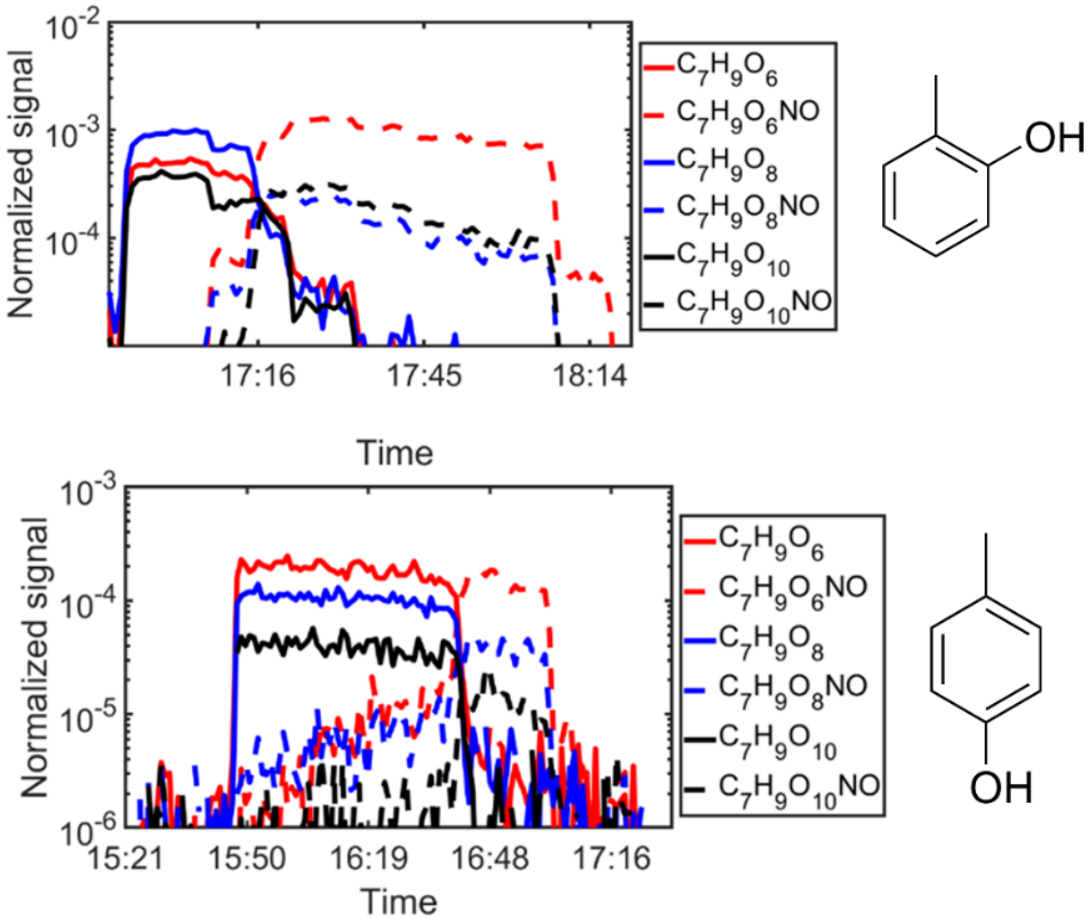

Fig. S33: cresol + OH + NO experiment: Residence time 1.9s. The HOM react with NO to form organonitrates, verifying that they are indeed peroxy radicals. This is seen as a decrease of the HOM signal and a simultaneous increase in the corresponding organonitrate signal.

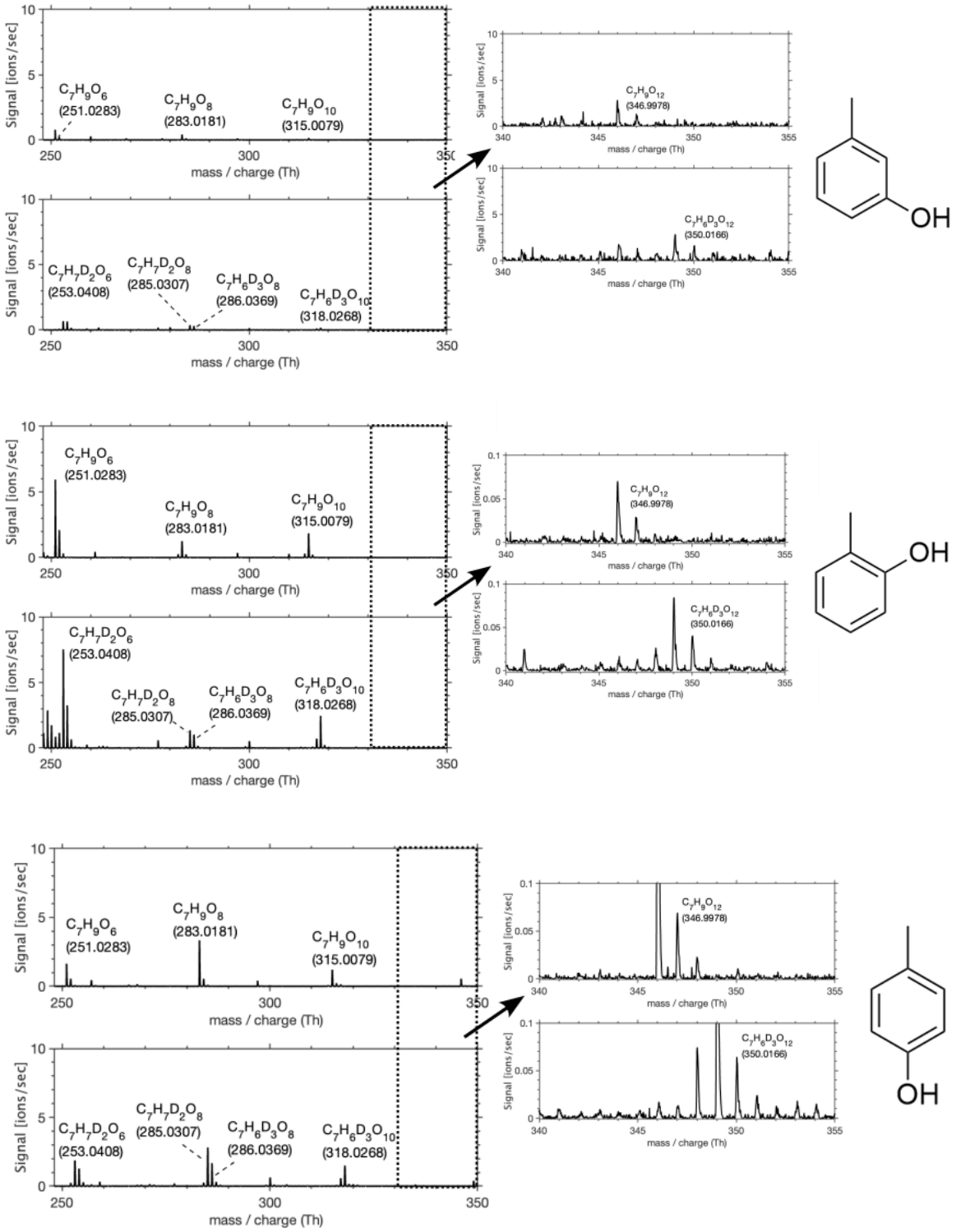

Fig. S34: Cresol + OH + D_2O experiments: The shift in the masses of the compound is seen as D_2O is added. This is due the labile H-atoms being replaced by heavier D-atoms. This provides information about the functional groups contained in the molecule.

The D_2O-experiments are seen in Fig. S34. The O_6-compounds generally have two isomers, one with two and one with three labile H-atoms. The same is seen for the O_8 compounds. For both of these, the dominant peak is the isomer with two labile H-atoms. For the O_{10} compounds,

only isomers with three labile H-atoms are seen. Also, for the O_{12} compounds, only three H-shifts are seen. 4 labile H-shifts would be expected for peroxy radical chemistry, as fitting 12 oxygen atoms onto a 7 carbon backbone, ring-broken or not, would require either trioxide formation, multiple ester/acylperoxy group possibly combined with heterocyclic ring-closure. No pathways to the formation of such compounds from aromatic oxidation are known but these could exist. It is also possible that the O_{12}-compounds are not fully deuterated due to the small concentration of molecules and short reaction times of the experiments. The presence of the O_6-compounds with 3 labile H-atoms could form as a result of H-shifts from the methyl group for cresols and other alkylbenzenes presented in Fig. S35. This is in apparent contradiction to the D_2O-experiments using NO_3^--CIMS for toluene, the simplest alkylbenzene, in which the corresponding O_5-compounds with two labile H-atoms were not seen [7]. This is expected, however, as very small amounts of O_5-compounds in general were observed due to the weak clustering with the NO_3^--ion. The corresponding O_6 compounds from cresol oxidation are likely much more prone to cluster with the NO_3^--ion due to the presence of two OH-groups compared to just one for toluene. This methyl-H-shift pathway is unlikely to lead to the observed O_{10} or O_{12} compounds as any ring-retaining O_{10}-compounds forming as a result of a H-shift would have either 4 or 5 labile H-atoms, neither of which is seen experimentally.

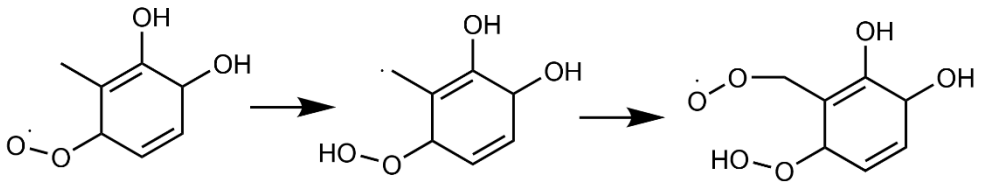

Fig. S35: Possible way to form O_6-compounds from o-cresol

S21: Orbitrap experiments

In addition to the NO_3^--experiments, another set of experiments were performed using Br^- as a reagent ion. The peak list is presented in Table S22 and the time series are seen in Fig. S36. The experiments were conducted at room temperature and atmospheric pressure using a flow reactor setup connected to Orbitrap Exploris 120 and 240 high-resolution mass spectrometers (Thermo Fisher Scientific). The experiments were performed at a 2.3 second reaction time. Oxidation experiments were conducted using ortho-, meta-, and para-cresol vapors as precursors. The liquid cresol (Meta: Sigma-Aldrich 99 %, Ortho: TCI - Tokyo Chemical Industry > 99.0 %, Para: Sigma-Aldrich ≥ 99.0 %) samples were vaporized by bubbling a controlled flow of nitrogen gas through the liquid reservoir. Two oxidants were used in the experiments: ozone (O3) and tetramethylethylene (TME). Ozone was generated from synthetic air via ultraviolet light irradiation using an ozone generator (UVP Ozone Generator, Analytik Jena US). The flow rate through the ozone generator was set to 1000 standard cubic centimeters per minute, resulting in an O3 concentration of approximately 400 ppb. TME was introduced into the system from a gas cylinder, with a concentration of 32 ppm. The oxidants and cresol vapor were mixed with synthetic air and introduced into a glass flow reactor under atmospheric conditions. TME reacts rapidly with ozone to produce hydroxyl (OH) radicals, which initiate the autoxidation of cresols. The formation of glyoxylic acid is seen for all of the cresol isomers.

This is in agreement with our mechanism of the C_1 oxidation pathway, but is not a conclusive verification as we cannot rule out other pathways to the formation of glyoxylic acid.

Table S22: cresol + OH Br^--CIMS spectra: Glyoxylic acid

Peak	Compound name	Peak
C2H2O2Br-	Glyoxal	136.924
C4H4O2Br-	Methylglyoxal	150.940
C2H2O3Br-	Glyoxylic acid	152.919
C3H4O3Br-	Methylglyoxylic acid	166.934

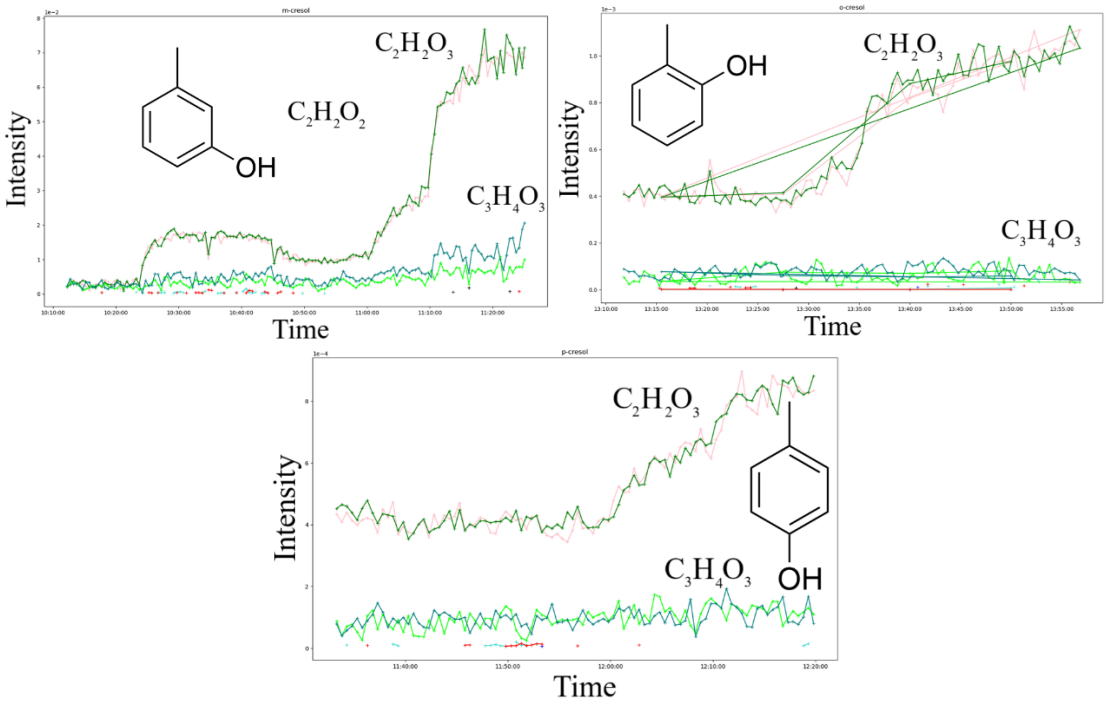

Fig. S36: cresol + OH Br^--CIMS time series: The peak corresponding to glyoxylic acid is seen to increase when cresols are added, whereas very little change is seen in the methylglyoxylic acid peak. Glyoxal and methyl glyoxal are detected only as small, occasional signals.

S22: 2-Naphtol experiments

In addition to the experiments to study cresol, experiments were also performed to study the oxidation products of 2-naphtol. TME ozonolysis was used as a source of OH radicals, similar to section S21, but this time the atmospheric pressure interface time-of-flight mass spectrometer was used in place of the Orbitrap mass spectrometer. The spectrum is seen in Fig. S37. The product distribution is very similar to that of the cresol isomers, with the spectrum being dominated by radical compounds with an even number of oxygen atoms. The chemical formulae and the short reaction time of 0.7s requires a fast autoxidation mechanism to the formation of these compounds that is initiated by OH-addition. Due to the similarity of aromatic autoxidation pathways in general, it is likely that the 2-naphtol HOMs form as a result of molecular rearrangement of BPRs. In analogy with the molecular rearrangement rates of cresols and other aromatics [2], molecular rearrangement rates are likely slow for BPRs formed

from OH-addition to non-substituted carbon atoms of 2-naphtol. The only substituted carbons atoms are the OH-substituted carbon (pos. 1 using notation of section S14), or the tertiary carbon atoms (pos. 4 and 9). OH-addition yields to the tertiary carbons are extremely low as seen in Table S12. This leaves the geminal diol pathway as the only known oxidation pathway that can explain the observed HOMs.

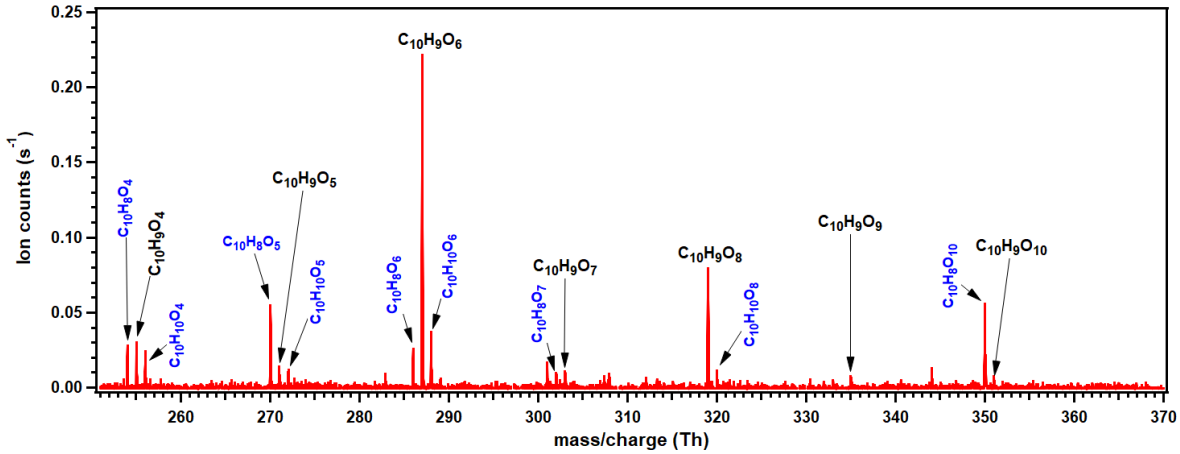

Fig. S37: 2-Naphtol oxidation experiments: Similar oxidation products are seen as in the cresol-experiments, with the main peaks being dominated by compounds with an even number of oxygen atoms. The reaction time is 0.7s, TME ozonolysis is used as a source of OH radicals.

References

1. Rate constants for the reactions of hydroxyl radicals and ozone with cresols at 300 ±1 K, Roger Atkinson, Karen R. Darnall, and James N, Pitts Jr. The Journal of Physical Chemistry 1978 82 (26), 2759-2761, DOI: 10.1021/j100515a001
2. Møller, K.H., Bates, K.H. and Kjaergaard, H.G., 2019. The importance of peroxy radical hydrogen-shift reactions in atmospheric isoprene oxidation. The Journal of Physical Chemistry A, 123(4), pp.920-932
3. J R Barker, A L Steiner, and T J Wallington. Advances in Atmospheric Chemistry. WORLDSCIENTIFIC, 2019. p. 409
4. Wu, PengZhen & Li, Jian & Li, Shujin & Tao, Fu-Ming. (2011). Theoretical study of mechanism and kinetics for the addition of hydroxyl radical to phenol. Science China Chemistry. 55. 10.1007/s11426-011-4380-1.
5. Olariu, Romeo & Klotz, Björn & Barnes, Ian & Becker, Karl & Mocanu, Raluca. (2002). FT–IR study of the ring-retaining products from the reaction of OH radicals with phenol, o-, m-, and p-cresol. Atmospheric Environment. 36. 3685-3697. 10.1016/S1352-2310(02)00202-9.
6. Jørgensen, Solvejg. (2012). Gas Phase Oxidation of Cresol Isomers Initiated by OH or NO3 Radical in the Presence of NO2. International Journal of Chemical Kinetics. 44. 165. 10.1002/kin.20703.
7. Iyer, S., Kumar, A., Savolainen, A. et al. Molecular rearrangement of bicyclic peroxy radicals is a key route to aerosol from aromatics. Nat Commun 14, 4984 (2023). https://doi.org/10.1038/s41467-023-40675-2

8. Lu Xu, Kristian H. Møller, John D. Crounse, Henrik G. Kjaergaard, and Paul O. Wennberg, Environmental Science & Technology 2020 54 (21), 13467-13477, DOI: 10.1021/acs.est.0c04780
9. Liming Wang, Runrun Wu, and Cui Xu, The Journal of Physical Chemistry A 2013 117 (51), 14163-14168, DOI: 10.1021/jp4101762
10. David R. Glowacki, Chi-Hsiu Liang, Christopher Morley, Michael J. Pilling, and Struan H. Robertson, The Journal of Physical Chemistry A 2012 116 (38), 9545-9560, DOI: 10.1021/jp3051033
11. Knispel, R., Koch, R., Siese, M. and Zetzsch, C. (1990), Adduct Formation of OH Radicals with Benzene, Toluene, and Phenol and Consecutive Reactions of the Adducts with NOx and O2. Berichte der Bunsengesellschaft für physikalische Chemie, 94: 1375-1379. https://doi.org/10.1002/bbpc.199000036
12. Zhang, Zhijie & Lin, Ling & Wang, Liming. (2012). Atmospheric oxidation mechanism of naphthalene initiated by OH radical. A theoretical study. Physical chemistry chemical physics : PCCP. 14. 2645-50. 10.1039/c2cp23271e.
13. Xu, Cui & Wang, Liming. (2013). Atmospheric Oxidation Mechanism of Phenol Initiated by OH Radical. The journal of physical chemistry. A. 117. 10.1021/jp308856b.
14. Santiago Olivella, Albert Solé, and Josep M. Bofill, Journal of Chemical Theory and Computation 2009 5 (6), 1607-1623, DOI: 10.1021/ct900082g
15. Iyer, S., Rissanen, M.P., Valiev, R. et al. Molecular mechanism for rapid autoxidation in α-pinene ozonolysis. Nat Commun 12, 878 (2021)
16. Taylor, Peter, Mechanism and Synthesis, 2003, The Royal Society of Chemistry, https://doi.org/10.1039/9781847557858-00005
17. Semadeni, M., Stocker, D.W. and Kerr, J.A. (1995), The temperature dependence of the OH radical reactions with some aromatic compounds under simulated tropospheric conditions. Int. J. Chem. Kinet., 27: 287-304. https://doi.org/10.1002/kin.550270307
18. Roger Atkinson, Karen R. Darnall, and James N. Pitts Jr., The Journal of Physical Chemistry 1978 82 (26), 2759-2761, DOI: 10.1021/j100515a001
19. Atkinson, R. and Aschmann, S.M. (1990), Rate constants for the gas-phase reactions of the OH radical with the cresols and dimethylphenols at 296 ± 2K. Int. J. Chem. Kinet., 22: 59-67. https://doi.org/10.1002/kin.550220105
20. R. A. Perry, R. Atkinson, and J. N. Pitts Jr., The Journal of Physical Chemistry 1977 81 (17), 1607-1611, DOI: 10.1021/j100532a001
21. Schwantes, Rebecca H & Schilling, Katherine & McVay, Renee C & Hakulinen, Hanna & Coggon, Mandy & Zhang, Xuan & Wennberg, Paul O & Seinfeld, John H. (2017). Formation of highly oxygenated low-volatility products from cresol oxidation. Atmospheric Chemistry and Physics. 17. 3453-3474. 10.5194/acp-17-3453-2017
22. Wu, PengZhen & Li, Jian & Li, Shujin & Tao, Fu-Ming. (2011). Theoretical study of mechanism and kinetics for the addition of hydroxyl radical to phenol. Science China Chemistry. 55. 10.1007/s11426-011-4380-1.
23. Sun, Yanhui & Xu, Fei & Li, Xiaofan & Zhang, Qingzhu & Gu, Yuanxiang. (2019). Mechanisms and Kinetic Studies of OH-initiated Atmospheric Oxidation of Methoxyphenols in the Presence of O2 and NOx. Physical Chemistry Chemical Physics. 21. 10.1039/C9CP03246K.
24. 1. Junninen, H.; Ehn, M.; Petäjä, T.; Luosujärvi, L.; Kotiaho, T.; Kostiainen, R.; Rohner, U.; Gonin, M.; Fuhrer, K.; Kulmala, M.; Worsnop, D. R. A high-resolution mass

spectrometer to measure atmospheric ion composition, *Atmos. Meas. Tech.* **2010**, *3*, 1039-1053.
25. 2. Hyttinen, N.; Kupiainen-Määttä, O.; Rissanen, M. P.; Muuronen, M.; Ehn, M.; Kurtén, T. Modeling the Charging of Highly Oxidized Cyclohexene Ozonolysis Products Using Nitrate-Based Chemical Ionization, *J. Phys. Chem. A* **2015**, *119*, 6339–6345.
26. C. Bloss, V. Wagner, M. E. Jenkin, R. Volkamer, W. J. Bloss, J. D. Lee, D. E. Heard, K. Wirtz, M. Martin-Reviejo, G. Rea, J. C. Wenger, and M. J. Pilling. Development of a detailed chemical mechanism (MCMv3.1) for the atmospheric oxidation of aromatic hydrocarbons. *Atmos. Chem. Phys.*, 5(3):641–664, 2005.
27. A. Guenther, X. Jiang, C. L. Heald, T. Sakulyanontvittaya, T. Duhl, L. K. Emmons, and X. Wang. The model of emissions of gases and aerosols from nature version 2.1 (MEGAN2.1): an extended and upyeard framework for modeling biogenic emissions. *Geosci. Model Dev.*, 5(6):1471–1492, 2012.
28. M. Jang and R. Kamens. Characterization of secondary aerosol from the photooxidation of toluene in the presence of NOx and 1-propene. *Env. Sc. and Tech.*, 35:3626–3639, 2001.
29. M. E. Jenkin, S. M. Saunders, V. Wagner, and M. J. Pilling. Protocol for the development of the Master Chemical Mechanism, MCM v3 (Part B): tropospheric degradation of aromatic volatile organic compounds. *Atmos. Chem. Phys.*, 3(1):181–193, 2003.
30. V. Lannuque, B. D'Anna, F. Couvidat, R. Valorso, and K. Sartelet. Improvement in modeling of oh and ho2 radical concentrations during toluene and xylene oxidation with racm2 using mcm/gecko-a. *Atmosphere*, 12(6):732, 2021.
31. V. Lannuque, B. D'Anna, E. Kostenidou, F. Couvidat, A. MartinezValiente, P. Eichler, A. Wisthaler, M. Mu¨ller, B. Temime-Roussel, R. Valorso, and K. Sartelet. Gas–particle partitioning of toluene oxidation products: an experimental and modeling study. *Atmos. Chem. Phys.*, 23:15537–15560, 2023.
32. P. B. Myrdal and S. H. Yalkowsky. Estimating pure component vapor pressures of complex organic molecules. *Industrial 'I& 'Engineering Chemistry Research*, 36(6):2494–2499, 1997.
33. Y. Nannoolal, J. Rarey, D. Ramjugernath, and W. Cordes. Estimation of pure component properties: Part 1. estimation of the normal boiling point of non-electrolyte organic compounds via group contributions and group interactions. *Fluid Phase Equilibria*, 226:45–63, 2004.
34. T. Sarica, K. Sartelet, Y. Roustan, Y. Kim, L. Lugon, B. Marques, B. D'Anna, C. Chaillou, and C. Larrie. Sensitivity of pollutant concentrations in urban streets to asphalt and traffic-related emissions. *Environ. Poll.*, 332:121955, 2023.
35. K. Sartelet, F. Couvidat, Z. Wang, C. Flageul, and Y. Kim. SSH-Aerosol v1. 1: A Modular Box Model to Simulate the Evolution of Primary and Secondary Aerosols. *Atmosphere*, 11(5):525, 2020.
36. K. Sartelet, Y. Kim, F. Couvidat, M. Merkel, T. Pet¨aj¨a, J. Sciare, and A. Wiedensohler. Influence of emission size distribution and nucleation on number concentrations over Greater Paris. *Atmos. Chem. Phys.*, 22(13):8579–8596, 2022.
37. K. Sartelet, Z. Wang, Y. Kim, V. Lannuque, and F. Couvidat. Advanced modeling of gas chemistry and aerosol dynamics with SSH-aerosol v2.0. *EGUsphere*, 2025:1–41, 2025.

38. K. Sartelet, Z. Wang, V. Lannuque, S. Iyer, F. Couvidat, and T. Sarica. Modelling molecular composition of soa from toluene photo-oxidation at urban and street scales. *Environ. Sci.: Atmos.*, 4:839–847, 2024.
39. D. Topping, M. Barley, M. K. Bane, N. Higham, B. Aumont, N. Dingle, and G. McFiggans. Umansysprop v1.0: an online and open-source facility for molecular property prediction and atmospheric aerosol calculations. *Geoscientific Model Development*, 9(2):899–914, 2016.
40. S. Wang, R. Wu, T. Berndt, M. Ehn, , and L. Wang. Formation of Highly Oxidized Radicals and Multifunctional Products from the Atmospheric Oxidation of Alkylbenzenes . *Env. Sc. and Tech.*, 51:8442–8449, 2017.
41. Z. Wang, F. Couvidat, and K. Sartelet. Implementation of a parallel reduction algorithm in the GENerator of reduced Organic Aerosol mechanisms (GENOA v2.0): Application to multiple monoterpene aerosol precursors. *J. Aerosol Sci.*, 174:106248, 2023.